The Wind-Driven Ocean Circulation with an Isopycnal-Thickness Mixing Parameterization

JAMES C. MCWILLIAMS AND PETER R. GENT

National Center for Atmospheric Research, Boulder, Colorado

(Manuscript received 11 August 1992, in final form 19 January 1993)

ABSTRACT

Numerical solutions are examined for the nearly adiabatic, large-scale ocean circulation in a midlatitude, rectangular domain with steady wind driving. The model used is the balance equations and its various subsets; hence, dynamical effects at finite Rossby number are included. The solutions are steady ones, and the necessary transports by the missing mesoscale eddies are parameterized, in part, using the authors' previous proposal for isopycnally oriented mixing of tracers and isopycnal thickness or static stability. This yields qualitatively credible, quasi-adiabatic solutions for realistic magnitudes for the subgrid-scale transport coefficients. Among these solutions are ones with nearly homogeneous fields of potential vorticity on upper-thermocline isopycnal surfaces, even though the parameterized eddy mixing does not act directly to this end.

1. Introduction

In this paper, we reexamine a classical problem of oceanography: the adiabatic, wind-driven time-averaged circulation in a midlatitude basin of simple shape and with a simple equation of state. The novel aspect here is a parameterization of mesoscale-eddy buoyancy transports that we have previously proposed (Gent and McWilliams 1990; hereafter abbreviated as GM90), namely, a quasi-adiabatic mixing along isopycnal surfaces of the static stability or, equivalently, the thickness between isopycnal surfaces. In addition, we use conventional parameterizations for subgrid-scale momentum transports: a horizontal eddy viscosity representing the mesoscale eddies and simple stress laws for the top and bottom planetary boundary layers. Given these parameterizations, the only relevant solutions for steady wind driving are steady ones; otherwise, the transient eddies would be, redundantly, both calculated and parameterized. Steadiness is assured by choosing the transport coefficients large enough such that the steady solutions are stable; however, they are not so large that the solutions are linear for a wind stress of realistic magnitude.

We obtain our solutions from the balance equations (BE) and their subset, the linear balance equations (LBE), which we believe may be sufficiently accurate models for the oceanic general circulation with its finite Rossby number. The LBE and BE are more accurate than the simpler quasigeostrophic equations (QG), whose approximations to the Coriolis force, in particular, are too severe in large basins, and they excise the extraneous degrees of freedom present in the more commonly used primitive equations. Balanced solutions that resolve the mesoscale eddies for this problem are presented in McWilliams et al. (1990; hereafter abbreviated as MNGH) and they can be viewed as extensions of many analogous solutions obtained with QG (e.g., Holland 1986).

In some sense it is a step backwards to examine steady (eddyless) solutions for a problem where eddy-resolving solutions are feasible. Nevertheless, our motivations for doing so are threefold: 1) the quality of an eddyless solution with parameterized eddy transports provides a measure of our understanding of their effects in the general circulation; 2) there are very few published, eddyless solutions for the baroclinic, wind-driven circulation in a simple basin that provide a framework for understanding its dynamics (but some examples are Welander 1966; Young and Rhines 1982; Ierley and Young 1983); and 3) it is not yet, and for many years will not be, computationally feasible to routinely calculate eddy-resolving solutions for the more general problem of the fully diabatic circulation with unsteady forcing in the complex geometry of the global ocean with the real equation of state. Thus, useful eddy parameterizations are needed for models of the general circulation, and the solutions herein allow at least a partial assessment of the GM90 proposal. In doing so, we can also make an assessment of the related proposal for a parameterized vertical eddy viscosity (Greatbatch and Lamb 1990), and we further show that there can be similarity in the effects of isopycnal mixing with the various proposals that eddies mix potential vorticity (PV) in wind-driven circulation (Marshall 1981, 1984; McWilliams and Chow 1981; Rhines and Young 1982a; Holland et al. 1984).

Corresponding author address: Dr. James C. McWilliams, NCAR, P.O. Box 3000, Boulder, CO 80307-3000.

The idea of PV mixing by eddies has numerous antecedents, primarily within the QG approximation (e.g., Rhines 1977), and it has many advocates. To date, however, there has been no parameterization proposal that extends this idea to the finite Rossby numbers of the general circulation.[1] In particular, choices must be made both for the particular definition of potential vorticity to be mixed (i.e., at what order of Rossby number it is to be approximated) and for the partition of its mixing terms between the buoyancy and momentum equations since no model at finite Rossby number is complete entirely within a potential vorticity equation. The GM90 parameterization form has nonconservative terms in the buoyancy equation. By itself it is not necessarily inconsistent with PV mixing, but with the simple form of momentum diffusion we use here, it is inconsistent. Perhaps a further refinement of GM90 to establish consistency with PV mixing may be attractive in the future, but our more immediate purpose is to address the following essential dynamical requirement for the general circulation.

The depth-averaged, or barotropic, circulation is strongly constrained to be close to the simple Sverdrup solution (Sverdrup 1947) on large horizontal scales, but the determination of the baroclinic structure of the circulation is more problematic. Consideration of the integral vorticity budget indicates that the surface wind torque must be balanced through horizontal and bottom boundary stresses; however, unless the flow is to be singularly trapped against the upper surface, some process must act to convey the circulation downward to make contact with, hence support a stress against, the lower boundaries. In an eddyless solution, it is perhaps natural to posit a vertical eddy viscosity for this process, representing the subgrid-scale vertical Reynolds stress. However, an estimate for the required viscosity, $\nu_v \sim h\tau/V$, is on the order of 1 $m^2\ s^{-1}$ for typical magnitudes of the wind stress and circulation depth scale and speed (see section 4), and this is larger by many orders of magnitude than observational estimates of ν_v (Gregg 1987). The GM90 parameterization represents an alternative regulator of the baroclinic structure, sometimes referred to as isopycnal form stress (because it arises from differential pressure forces on the convoluted surfaces of constant density). A different view of this process is that the parameterized eddy fluxes maintain an ageostrophic circulation that acts through the Coriolis force to effect the downward penetration of the circulation. The required transport coefficients for this isopycnal mixing process are not unphysically large.

This mechanism is missing in standard, eddyless oceanic general circulation models, and its lack is compensated for, usually not by resort to unphysically large ν_v, but rather by inclusion of horizontal (rather than isopycnal) tracer diffusivities. The latter coincides with our isopycnal mixing parameterization to leading order in Rossby number, but it has the undesirable and often substantial diabatic consequence of diffusing away the buoyancy stratification due to the tilting of isopycnal surfaces at the finite Rossby numbers of the large-scale circulation. Furthermore, a simple rotation of the tracer diffusivity tensor to be tangent to isopycnal surfaces (Redi 1982) would not suffice for achieving an equilibrium vorticity balance, since its dynamic effect disappears when buoyancy is a function of only one tracer (as with our simple equation of state here).

[1] We exclude the planetary geostrophic approximation, with its linear diagnostic momentum balance, as insufficiently accurate, particularly in boundary currents.

2. Balanced and quasigeostrophic equations

Here we present the equations and boundary conditions for the BE in nondimensional, continuous form and then identify the subsets of the BE that make up the simpler models LBE and QG. The formal properties of balanced models are analyzed in Gent and McWilliams (1983a,b). Particular examples of consistent boundary-value problems and numerical solution methods are presented for the BE in a horizontally periodic, β-plane domain in Norton et al. (1986) and for the LBE in a closed domain with general $f(y)$ in MNGH. The presentation here parallels section 2 of MNGH but is generalized to the BE with the isopycnal mixing parameterization.

The nondimensionalization is of the classical QG type. The fundamental scaling quantities are l_* for horizontal coordinates (x, y), h_* for vertical coordinate z, V_* for horizontal velocities (u, v), f_* for Coriolis frequency, and N_* for mean (i.e., horizontally averaged) buoyancy (Brunt–Väisälä) frequency. (The subscript asterisk denotes a dimensional value.) These scales are combined in the nondimensional Rossby and Burger numbers,

$$R = \frac{V_*}{f_* l_*}, \quad B = \left(\frac{N_* h_*}{f_* l_*}\right)^2. \tag{1}$$

Other quantities are made nondimensional by appropriate combinations of the fundamental scales; for example, the time t is scaled by l_*/V_*.

a. Velocity and buoyancy fields

The horizontal velocities are decomposed into rotational and divergent components,

$$u = -\psi_y - RX_{xz}, \quad v = \psi_x - RX_{yz}, \tag{2}$$

with streamfunction ψ and velocity potential X. (Independent variable subscripts denote derivatives.) The vertical component of vorticity ζ is $v_x - u_y$; thus, (2) implies

$$\nabla^2\psi = \zeta, \tag{3}$$

where ∇^2 is the horizontal Laplacian operator. The vertical velocity w is scaled by $V_*^2 h_*/f_* l_*^2$. The incompressibility relation can thus be written as

$$w_z = -\frac{u_x + v_y}{R} = \nabla^2 X_z. \tag{4a}$$

This has a simple vertical integral consistent with no flow through the vertical boundaries:

$$w = \nabla^2 X. \tag{4b}$$

The buoyancy field is assumed to be proportional to the temperature field here, and T is decomposed into a horizontally averaged component $\Theta(z, t)$, with dimensional scale $h_* N_*^2/g_* A_*$, and its deviation component $\theta(x, y, z, t)$, with scale $f_* l_* V_*/g_* h_* A_*$, where $g_* = 9.8$ m s^{-2} is the gravitational acceleration and $A_* = 2 \times 10^{-4}$ K^{-1} is the coefficient of thermal expansion in the linear equation of state. In addition, these fields are related to the area-averaged stability profile S and the geopotential ϕ:

$$T = \frac{B}{R}\Theta + \theta, \quad S = B\Theta_z, \quad \phi_z = \theta. \tag{5}$$

We need not be concerned with an area-averaged geopotential function in hydrostatic balance with Θ, because no motion is associated with it.

b. *Vorticity equation*

The horizontal momentum balance in the BE is supplanted by its curl and divergence. The former is the vorticity equation,

$$\zeta_t = -J(\psi, \zeta + \delta f) + \nabla \cdot f\nabla X_z + R\nabla\cdot(\nabla^2\psi\nabla X_z - \nabla^2 X\nabla\psi_z) + \mathcal{G} + \mathcal{F}_z, \tag{6a}$$

where J and ∇ are the horizontal Jacobian and gradient operators, respectively. Other quantities in (6a) are defined by

$$f = 1 + R\beta(y - y_c),$$
$$\delta f = \beta(y - y_c),$$
$$\mathcal{G} = \nu_h \nabla^2 \zeta,$$
$$\mathcal{F} = \nu_v \zeta_z, \tag{6b}$$

where β is the y gradient of the Coriolis frequency f, y_c is the meridional midpoint of the domain, and the ν are horizontal and vertical viscosities. The domain is rectangular with $0 \leq x \leq L_x$, $0 \leq y \leq L_y$, $0 \leq z \leq H$.

On the horizontal boundary $\delta\mathcal{B}$, the boundary conditions associated with (6a) are the inviscid conditions of no normal flow,

$$\psi = 0, \quad X_n = 0, \tag{6c}$$

and the viscous condition of tangential stress proportional to tangential velocity,

$$\psi_{nn} = -\alpha\psi_n, \tag{6d}$$

where (n, s) is a rotation of (x, y) oriented outwardly normal to the horizontal boundary. Vertical boundary conditions associated with (6a) are the inviscid condition of no vertical flow and the viscous conditions associated with wind stress τ_s at the top and turbulent boundary-layer drag at the bottom:

$$X(0) = X(H) = 0, \quad \mathcal{F}(H) = \text{curl}\,\tau_s,$$
$$\mathcal{F}(0) = \epsilon\zeta(0), \tag{6e}$$

where ϵ is the bottom drag rate.

c. *Thermal balance equation*

The divergence of the horizontal momentum equation yields the defining balance relation for the BE. In our formulation we need consider only its vertical derivative, which we call the thermal balance equation:

$$\nabla^2\theta = \nabla\cdot f\nabla\psi_z + 2R\frac{\partial}{\partial z}J(\psi_x, \psi_y), \tag{7a}$$

with its associated horizontal boundary condition,

$$\theta_n = f\psi_{nz}, \tag{7b}$$

on $\delta\mathcal{B}$, and integral normalization condition [n., (5)],

$$\langle\theta\rangle \equiv \frac{1}{L_x L_y}\int\int dxdy\theta = 0. \tag{7c}$$

For uniform validity in an expansion in R, there should be an extra term in (7b) (viz., $-RX_{zzs}$ on the right-hand side); however, to avoid a technical difficulty in our solution method, we do not include it here (and, as will be shown, the accuracy of our present solutions with respect to R is not in doubt).

d. *Buoyancy equations*

The buoyancy balance is decomposed, just as T in (5), into area-averaged and deviation equations. The former is

$$B\Theta_t = -R^2\langle w\theta\rangle_z + R\langle Q\rangle, \tag{8}$$

while the latter is

$$\theta_t = -J(\psi, \theta) - Sw + R[\nabla\cdot\theta\nabla X_z - (w\theta)_z + \langle w\theta\rangle_z] + Q - \langle Q\rangle. \tag{9}$$

The "quasi-adiabatic" buoyancy forcing term Q is discussed in section 3. No incremental boundary or integral conditions are required for (8) and (9) beyond those specified above. The boundary conditions of no normal flow (6c,e) and mass conservation (4b) imply that $w(0) = w(H) = 0$ and $\langle w\rangle = 0$.

e. *Simpler models*

The LBE are obtained from the BE [Eqs. (2)–(9)] simply by deleting the terms that appear in Eqs. (6a)

and (7a) with an explicit coefficient R. The QG model is a much smaller subset of the BE, defined by setting $R = 0$ and $f = 1$ in (6)–(9), while retaining $\delta f \neq 0$. The QG model has some substantial simplifications over LBE. For example, in this limit (7a) and (8) can be integrated explicitly:

$$\theta = \psi_z - \langle \psi_z \rangle, \quad \Theta(z, t) = \Theta(z, 0), \qquad (10)$$

assuming $\langle Q \rangle = 0$ (see below).

3. Isopycnal mixing parameterization

The parameterization scheme in GM90 represents isopycnally oriented fluxes of material properties by mesoscale eddies. This scheme is pointwise diabatic, in that material properties are not conserved on resolved-scale trajectories, but integrally adiabatic. For the present situation of the linear, single-component equation of state implicit in (5) and no tracers other than temperature, the parameterization reduces to a divergence in isopycnal coordinates of an isopycnally oriented flux in the mass-conservation equation. This flux is the density derivative of the product of a diffusivity, κ_i times the horizontal gradient of the height of an isopycnal surface [see (6) and (15) of GM90]. This is equivalent to a source term $Q = Q_i$ in the buoyancy equations (8)–(9) of the form

$$Q_i \equiv \nabla \cdot [\kappa_i \nabla T] - \frac{\partial}{\partial z}\left[\frac{\kappa_i \nabla T \cdot \nabla T}{T_z}\right], \qquad (11)$$

where all derivatives are in Cartesian coordinates (x, y, z). As discussed in GM90, this term usually acts on the resolved-scale motions to reduce horizontal differences in the thickness between neighboring isopycnals, to reduce available potential energy in a way that mimics baroclinic instability, and to transfer horizontal momentum vertically in a way that mimics isopycnal form stress. In particular, for spatially uniform κ_i in the QG approximation and away from vertical and horizontal boundaries, (11) contributes to the governing potential vorticity equation isomorphically to momentum diffusion $\mathcal{F}_z$ in (6a,b) with a nondimensional vertical viscosity,

$$\nu_v(z) = \kappa_i / S(z). \qquad (12a)$$

In the QG approximation (as $R \to 0$), the second term in (11) is neglected, and Q_i acts like a horizontal temperature diffusion, with $\langle Q_i \rangle = 0$ given the boundary condition (13) below.

This correspondence between ν_v and κ_i in QG also has an approximate analog for the planetary geostrophic equations (PG),

$$\nu_v = \frac{f^2(y)}{N^2(x, y, z, t)}\,\kappa_i, \qquad (12b)$$

where $N^2 \equiv S(z) + R\theta_z$. This led Greatbatch and Lamb (1990) to propose a vertical momentum diffusion parameterization for mesoscale eddy transports with the indicated spatial dependence for ν_v. This approximate correspondence requires both that terms of $O(\nu_v^2)$ be neglected and that in certain instances $R\delta f$ be neglected compared to 1 or f. Furthermore, it applies only to the forcing of the potential vorticity equation and thus not to the solution as a whole. Finally, even this approximate correspondence fails for more general models such as the BE. Our preference is for isopycnal buoyancy flux rather than vertical momentum flux as a parameterization basis, for the reasons indicated in the Introduction, even though comparable solutions, related by (12a,b), may often be quite similar in certain aspects (see section 4c).

The diabatic term (11) allows conservation of all the integral moments of the buoyancy field, $\int d\text{vol}\, T^m$, with suitably insulating boundary conditions. Here we use a consistent alternative to what was suggested in GM90 that is particularly suited to the discrete implementation of (11):

$$\kappa_i T_n = 0 \text{ on } \delta\mathcal{B}, \quad \kappa_i = 0 \text{ on } z = 0, H. \qquad (13)$$

The horizontal condition here is to be interpreted not as an extra condition on T but as a constraint on the discrete form of Q_i on the horizontal boundary. This is a less severe constraint than setting $\kappa_i = 0$ on $\delta\mathcal{B}$, which would also assure (13), although in practice solutions with these alternative boundary conditions are little different. The formulas (11) and (13) imply a systematic loss of potential energy:

$$\text{PE}_t = -\int d\text{vol}\, w\theta - \int d\text{vol}\, \frac{\kappa_i \nabla\theta \cdot \nabla\theta}{S + R\theta_z}, \qquad (14)$$

for $\text{PE} = -R^{-1} \int d\text{vol}\, zT$. The integrals here are to be taken as volume averages.

Finally, we also include, in some calculations, a fully diabatic component of Q for horizontal buoyancy diffusion on the top and bottom boundaries:

$$Q_h \equiv \nabla \cdot [\kappa_h \nabla T]\{\delta(z) + \delta(z - H)\}, \qquad (15)$$

where δ is equal to one when its argument is zero and zero otherwise. This term is not consistent with conservation of the integral moments of the buoyancy field. Its dynamical rationale is the following. Although $\theta \equiv 0$ at $z = 0$ and H is a correct solution to the fully adiabatic problem (see MNGH), it is not a unique one. If nonzero boundary $\theta(x, y, t)$ arises either through initial conditions (but not the ones we use here) or computational errors (which are inescapable at some level), or if there are quasi-adiabatic effects of Q_i for κ_i and $R \neq 0$, then the isothermal boundary solution will not be selected. Once present, the boundary θ field will evolve approximately as a passive tracer in the two-dimensional, nondivergent flow associated with the boundary ψ field (i.e., to leading order in R, there is no dynamical coupling to the interior fields). This evolution is a cascade to small scales, hence growth of

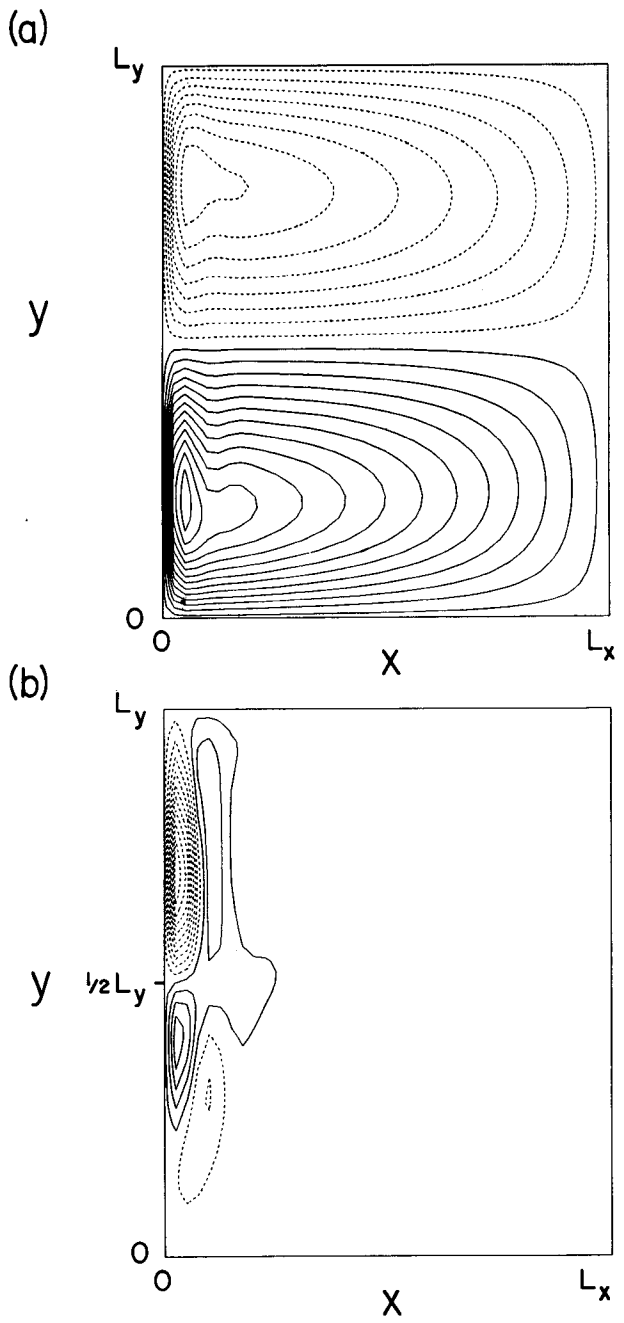

FIG. 1. Plot of $\psi(x, y, z_l)$ at $t = 200$ and $l = 6$ and 1 for the LBE solution of section 4a. The contour intervals are 0.1 and 0.005, respectively; negative and positive contours are dashed and solid lines, respectively; and the contour values symmetrically straddle zero.

$\langle(\nabla\theta)^2\rangle$. The role of (15), then, is to absorb this cascade by dissipating tracer variance and to establish a smooth boundary θ in a quasi-steady-state solution (i.e., one with only a slow dissipative evolution associated with a small $\kappa_h \neq 0$). The physical rationale for (15) is that it represents horizontal mixing by the 3D turbulence within the top and bottom planetary boundary layers. As we shall see (section 4b), Q_h is neither necessary for computational stability nor is its feedback onto the interior fields quantitatively significant here.

Discretization formulas for Q_i and Q_h that have the desired integral properties are presented in appendix B.

4. Solutions

a. A representative solution

First we examine a solution for typical parameter values. With the North Atlantic Ocean in mind, we consider a rectangular ocean basin with dimensions 4000 km × 5000 km × 5 km, centered at 38°N latitude, and driven by a steady, meridionally symmetric wind stress with a peak amplitude $\tau_{0*} = 10^{-4}$ m^2 s^{-2}. The initial buoyancy profile exponentially decays with depth on a scale of 800 m and has an associated first baroclinic radius of deformation of 45 km (which will be below the usual grid resolution scale of 100 km—see below). The horizontal viscosity is $\nu_{h*} = 0.75 \times 10^4$ m^2 s^{-1}; this is a large value appropriate to an eddyless solution. The horizontal boundaries have zero stress (i.e., $\alpha = 0$), and the velocity coefficient for bottom stress is $\epsilon_* = 2.65 \times 10^{-4}$ m s^{-1}. Only the vertical viscosity and diabatic diffusivities remain to be specified (see below).

The characteristic scales for nondimensionalization represent the large-scale circulation for the problem stated above:

$$l_* = 500 \text{ km}, \quad V_* = 0.1 \text{ m s}^{-1}, \quad h_* = 800 \text{ m},$$
$$f_* = 0.90 \times 10^{-4} \text{ s}^{-1}, \quad N_* = 7.63 \times 10^{-3} \text{ s}^{-1}. \tag{16}$$

These scales are used as in MNGH to define the nondimensional parameters that appear in the equations in section 2:

$$L_x = 8, \quad L_y = 10, \quad H = 6.25,$$
$$R = 2.22 \times 10^{-3}, \quad B = 0.018, \quad \beta = 42.2,$$
$$\nu_h = 0.15, \quad \epsilon = 1.66, \quad \alpha = 0. \tag{17}$$

The surface wind stress is

$$\tau_s = \mathbf{e}_x \tau_0 \cos\left[2\pi\left(\frac{y}{L_y} - \frac{1}{2}\right)\right], \tag{18}$$

with $\tau_0 = 6.25$. The initial buoyancy profile is

$$\Theta(z, 0) = e^{z-H} + \Theta_0, \tag{19}$$

where Θ_0 is a dynamically inconsequential constant; the dimensional, top to bottom temperature difference implied by (19) is 23 K, given (16). Other initial conditions are $\psi = \theta = 0$, representing an impulsive start-up from a state of no motion. The spatial discretization is on a grid of 40 × 50 × 6, unless stated otherwise.

Thus, the horizontal grid spacing is everywhere $da = 0.2$ (i.e., 100 km) and the staggered, stretched vertical grid levels are either $z_l = \{2.07, 3.73, 4.62, 5.24, 5.70, 6.08\}$, $l = 1, \cdots, 6$, for the ψ and **u** variables or $z_k = \{0, 3.06, 4.22, 4.95, 5.48, 5.90, 6.25\}$, $k = 0, \cdots, 6$, for the T and X variables. The time-step size is $dt = 0.017$ (i.e., 1 day).

We now examine an LBE solution for a problem as specified above. We choose to focus at first on the situation with no vertical viscosity, an isopycnal diffusivity not much larger than the critical value at which the solution approaches a steady state at late time, and as small a horizontal diffusivity as yields a marginally smooth boundary temperature field at late time; namely,

$$\nu_v = 0, \quad \kappa_i = 0.03, \quad \kappa_h = 0.01. \tag{20}$$

The κ have the same nondimensionalizing factor as ν_h [i.e., $V_* l_* = 5 \times 10^4$ m^2 s^{-1} from (16)]; thus, the effective Prandtl numbers ν/κ are large here, 5 for the isopycnal mixing and 15 for the horizontal mixing on the boundary. Neither these κ nor the ν_h above are inconsistent in magnitude with observational estimates for lateral diffusivities by mesoscale eddies (McWilliams et al. 1983).

The spinup from rest is relatively rapid, occurring over an interval of $\Delta t \sim 100$ [i.e., about 16 yr from (16)], and we will analyze the nearly steady-state solution at $t = 200$. The horizontal patterns of circulation are shown in Fig. 1 for both the shallowest and deepest levels. In the upper ocean, there is the familiar double gyre system, reflecting the pattern of wind driving (18). There is some enhanced recirculation near the western boundary; the latter is much stronger in the subtropical gyre because of the greater surface intensification of the flow there due to meridionally asymmetric effects of the Coriolis force or, equivalently, to the stronger stretching of planetary vorticity where $f(y)$ is larger (see also the discussion in MNGH). At the deepest level (Fig. 1b), however, the wind-driven gyres are absent, and there is only western-boundary recirculation, most intensely in a subpolar cyclonic gyre. These enhancements of near-boundary recirculation are nonlinear dynamical effects (cf. section 4d and appendix A).

The depth-averaged circulation $\bar{\psi}^z$ (Fig. 2a) shows only a weak meridional asymmetry (again as in MNGH). Furthermore, in all regions except near the western boundary, $\bar{\psi}^z$ corresponds quite well to the Sverdrup transport streamfunction ψ_{sv} (Sverdrup 1947),

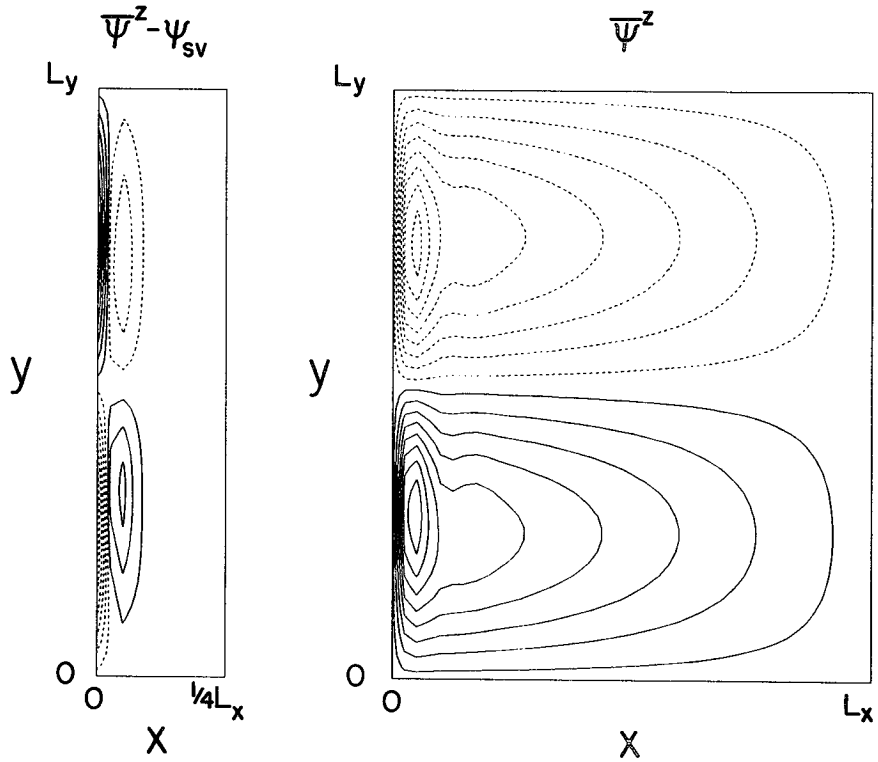

FIG. 2. The depth-averaged streamfunction, $\bar{\psi}^z(x, y)$, and its difference from ψ_{sv} [see (21)] in the western quarter of the domain. The contour interval is 0.02.

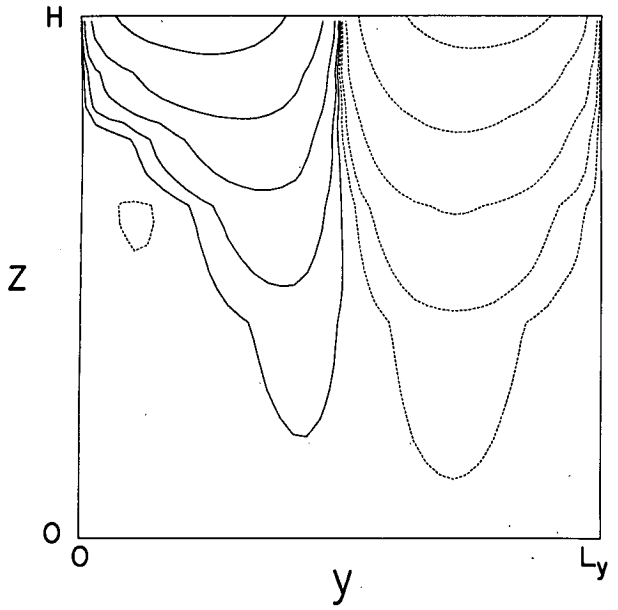

FIG. 3. The mean horizontal recirculation in the meridional plane, $\bar{\psi}^x(y,z)$, with geometrically increasing contours beginning at $\pm\sqrt{10} \times 10^{-3}$ and increasing in magnitude by the factor $\sqrt{10}$.

$$\psi_{sv}(x, y) = -C_{sv}\left(1 - \frac{x}{L_x}\right) \sin\left[2\pi \frac{y - y_c}{L_y}\right],$$

$$C_{sv} = \frac{2\pi L_x \tau_0}{\beta H L_y}, \tag{21}$$

as can be seen in Fig. 2b. The total circulation in each gyre is $H \cdot \Delta\bar{\psi}^z \approx 1.0$ [i.e., about $h_* l_* V_* = 40 \times 10^6$ $m^3\ s^{-1}$ from (16)], of which about one-third is an enhanced western-boundary recirculation above the Sverdrup circulation. A linear boundary-layer solution (appendix A) corresponds well to Fig. 2b in its spatial scale and location of extrema; however, the amplitude of the secondary extremum at $\Delta x \approx 0.4$, relative to the wall extremum, is underestimated by about 30%. One clear deficiency of our eddyless solution, compared to eddy resolving solutions as in MNGH, is that the separated western-boundary current, the "Gulf Stream," does not leave the coast in only a narrow latitude range nor does it penetrate very far in the zonal direction. Associated with this deficiency are recirculation zones and deep jets that also have excessively meridional orientations. A possible remedial approach is illustrated in section 4f.

The baroclinic structure of the gyres can be seen in meridional (Fig. 3) and zonal (Fig. 4) cross sections for $\bar{\psi}$, where the average is taken in the perpendicular horizontal coordinate. We note that the circulations are roughly exponential in their vertical profiles, with a depth scale that is somewhat larger in the subpolar gyre than in the subtropical one and that increases strongly from east to west. This depth scale is somewhat smaller than 1 [i.e., <800 m from (16)], and its absolute magnitude is substantially controlled by the initial stratification (19). Note that the depth scale deepens to the north in the subtropical gyre and vice versa in the subpolar gyre, as predicted in Rhines and Young (1982b).

There is also a divergent circulation (u_d, v_d, w), represented by the potential X in (2) and (4); it is weaker

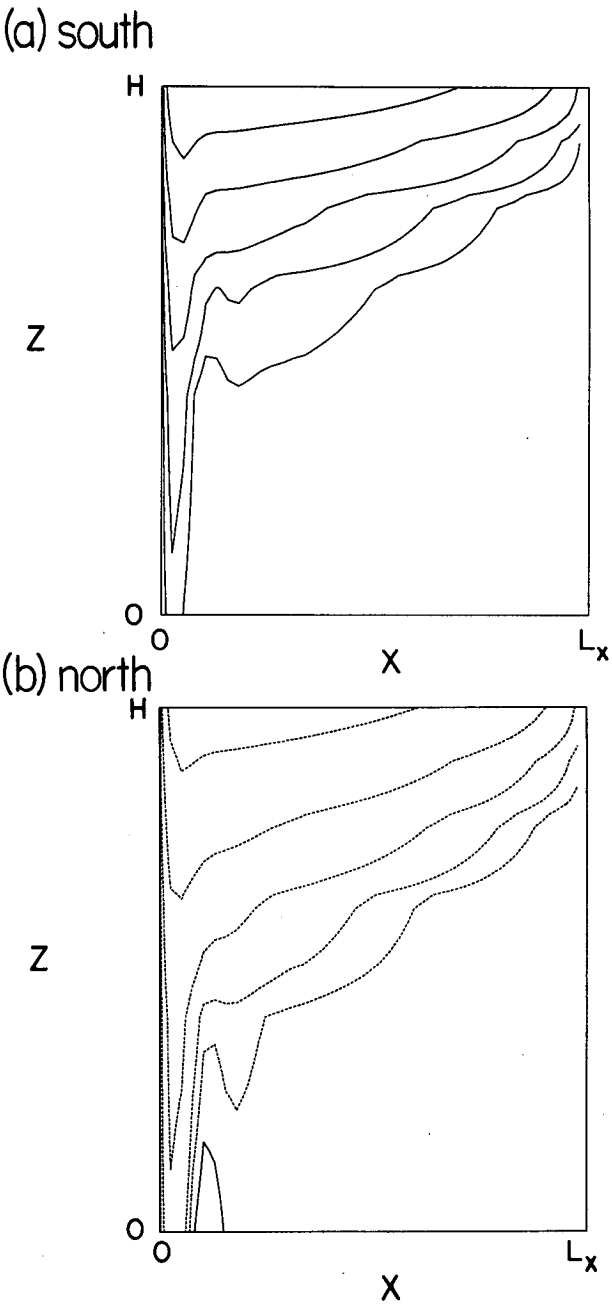

FIG. 4. The mean horizontal recirculation in the zonal planes, $\bar{\psi}^y(x, z)$, for the southern and northern halves of the domain, with geometrically increasing contours beginning at $\pm\sqrt{10} \times 10^{-3}$ and increasing in magnitude by the factor $\sqrt{10}$.

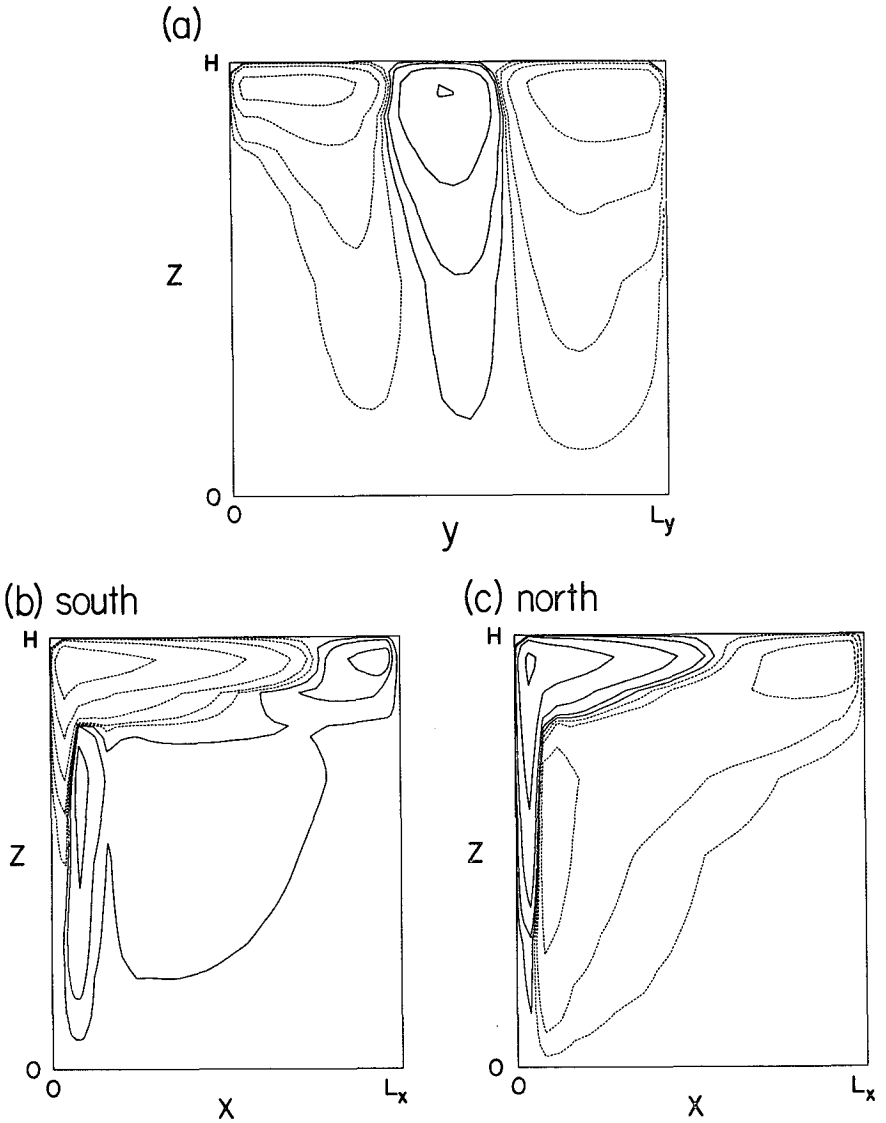

FIG. 5. The mean overturning circulations (a) in the meridional plane, $\xi^{(yz)}$ from (22), and, in the zonal planes, $\xi^{(xz)}$ from (23) for the (b) southern and (c) northern halves of the domain. The contours being at $\pm\sqrt{10} \times 10^{-2}$ and increase in magnitude geometrically by the factor $\sqrt{10}$.

than the ψ circulation by a factor of R but nevertheless plays an essential role in the dynamics. The mean meridional part of this circulation can be expressed in terms of a cross-sectional streamfunction $\xi^{(yz)}(y, z)$, defined by

$$\left[\frac{\partial^2}{\partial y^2} + \frac{\partial^2}{\partial z^2}\right]\xi^{(yz)} = \frac{\partial}{\partial z}\overline{v_d}^x - \frac{\partial}{\partial y}\bar{w}^x,$$

$$\xi^{(yz)} = 0 \text{ on } y, z \text{ boundaries}, \quad (22)$$

where $v_d \equiv -X_{yz}$ [see (2)]. Analogously, the mean, zonal, divergent circulation can be expressed in terms of a $\xi^{(xz)}(x, z)$, defined by

$$\left[\frac{\partial^2}{\partial x^2} + \frac{\partial^2}{\partial z^2}\right]\xi^{(xz)} = \frac{\partial}{\partial z}\overline{u_d}^y - \frac{\partial}{\partial x}\bar{w}^y,$$

$$\xi^{(xz)} = 0 \text{ on } x, z \text{ boundaries}, \quad (23)$$

where $u_d \equiv -X_{xz}$. When the horizontal average in (22) or (23) spans the basin, ξ defines the mean cross-sectional circulation exactly. We use such an average for the meridional circulation (22) in Fig. 5a, but we choose to separately average over the southern and northern halves of the domain for the zonal circulations (23) in Figs. 5b,c; since the basin midline coincides with curl$[\tau_s] = 0$ from (18) and approximately with a line of symmetry for the solution (see Figs. 1–5a),

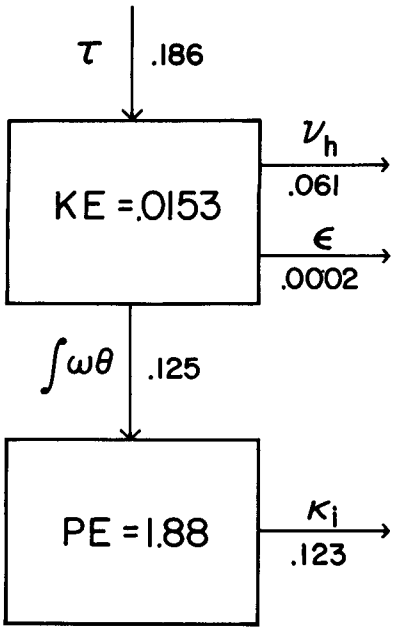

FIG. 6. Volume-integrated energetics at $t = 200$: kinetic and potential energy values are inside the boxes, and the labeled arrows denote the sign and magnitude of the work done by the associated processes. Definitions are as in MNGH, plus (14).

the part of the mean zonal circulation not represented in $\xi^{(xz)}$—that is, the degree to which the half-basin mean flow is not x, z nondivergent—is negligibly small. The sense of the ξ is such that the circulation is counterclockwise around a positive extremum.

In the meridional circulation for our solution (Fig. 5a), we see cells that are analogous to the Ferrel cell of the atmospheric jet stream (e.g., Lorenz 1967) or that of the Antarctic Circumpolar Current (McWilliams and Chow 1981): poleward flow beneath an upward-intensified eastward flow that undergoes baroclinic energy losses (here due to Q_i). This is the flow configuration that occurs in the central latitudes of the domain here, and its reverse occurs in the regions of westward flow on the edges. The zonal circulations (Fig. 5b,c) are approximately antisymmetric between the gyres, and within each gyre the strongest cell is driven by vertical motions in the upper portion of the western-boundary currents; the upward boundary motion in the subtropical gyre is somewhat stronger and more surface-intensified than its downward counterpart in the subpolar gyre. These features are also found in the linear boundary-layer solutions in appendix A. In addition, there is a weaker and wider cell of the opposite sign in each gyre, with distinct extrema in the deep western and in shallow eastern boundary currents.

The quasi-steady energy balance for this solution (Fig. 6) shows a kinetic energy cycle of wind work balanced about one-third by viscous dissipation (mostly horizontal because the deep circulation is so weak here; Fig. 1b) and two-thirds by conversion to potential energy. The potential energy is fed by the latter conversion process slightly in excess of its loss through the isopycnal mixing term (14), and the small imbalance is due, indirectly, to the action of Q_h from

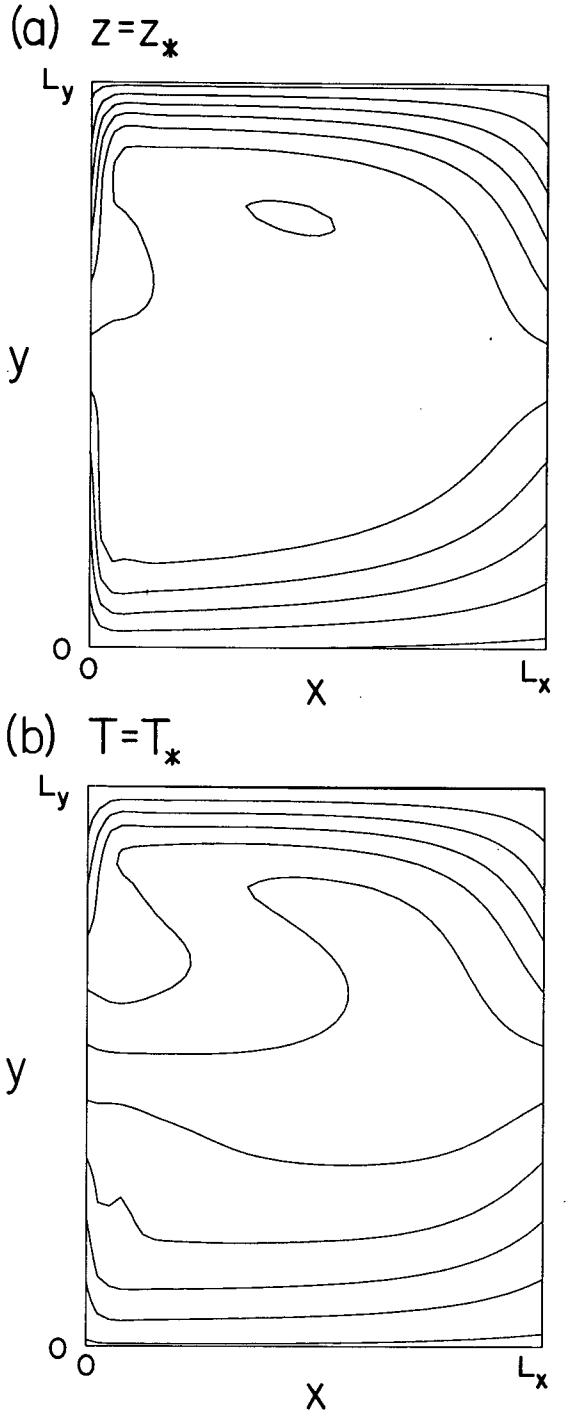

FIG. 7. Large-scale potential vorticity, PV $= fT_z$, at $t = 200$, with contours at an interval of 150 straddling the average value: (a) PV(x, y, z_*) for $z_* = 5.48$; (b) PV(x, y, T_*) for $T_* = 3.8$ (the average height of this T_* surface is 5.48).

(15). Here Q_h has no direct contribution to the energy balances in the sense that there is no term proportional to κ_h. However, the geostrophic tilting of interior isotherms away from horizontal planes and the connection to the vertical boundaries through κ_i establish T gradients there to be mixed by Q_h. This has the effect of diminishing the overall stratification, hence increasing PE, and it enters into the energy balance equations implicitly through the $\int w\theta$ conversion from KE to PE. The ultimate end state would be an isothermal ocean, although for the small κ_h in (20) the rate of approach is very slow, consistent with the small imbalance in the PE budget in Fig. 6. For this eddyless solution, we interpret the losses due to ν_h and κ_i as surrogates for the eddy generation terms in an eddy-resolving solution with smaller transport coefficients. In this sense the energy cycle in Fig. 6 is qualitatively plausible.

The large-scale potential vorticity is defined by

$$\mathrm{PV} = fN^2/R = R^{-1}[1 + R\delta f(y)][S(z) + R\theta_z]. \quad (24)$$

There is an expectation that PV should be homogeneous (i.e., spatially uniform) on isopycnal surfaces for the wind-driven circulation. The bases for this expectation are 1) the extrapolation to large horizontal scales and finite R of the QG results in adiabatic eddy mixing sometimes homogenizing potential vorticity on level surfaces (McWilliams and Chow 1981; Rhines and Young 1982a; Holland et al. 1984) and 2) the empirical demonstration that PV has only weak variations on isopycnal surfaces in the upper thermocline in midlatitude gyres (McDowell et al. 1982). For the present solution, the vertical region in which Q is most homogeneous is indeed the upper thermocline, and its horizontal distributions are shown in Fig. 7. Somewhat contrary to the expectation, however, PV is more homogeneous on a level surface (Fig. 7a) than on a nearby isopycnal surface (i.e., with constant T; see Fig. 7b). Of course, since our present solution lacks eddies but has their parameterized effects of $\mathcal{G}$, $\mathcal{F}$, and Q in forms that do not mix PV in any direct fashion, we have not biased a priori the degree of homogenization here. This issue is examined further in section 4e.

The temperature fields on the vertical boundaries are of particular interest in this nearly adiabatic context since they necessarily have $\theta \neq 0$ due to Q_i (see section 3). On the bottom surface (Fig. 8a), the temperature contrast is very slight, with $\Delta T \approx 0.003$ [i.e., about 0.01 K, from (5) and (16)]. On the top surface (Fig. 8b), however, the contrast is much larger, with $\Delta T \approx 1.5$ (i.e., about 4 K). The large-scale pattern is one of warm temperatures in the subtropical gyre and cold in the subpolar gyre; this reflects mixing from the subsurface fields with a similar pattern (i.e., resembling ψ in Fig. 1a). There are, however, two smaller-scale features: a cold pool in the southwestern portion of the subtropical gyre and a front across the gyre boundary that is much sharper in surface temperature than in streamfunction (Fig. 1a). The latter reflects the frontogenetic tendency for a passive-scalar gradient in a deformation velocity field, and it is likely relevant to the real ocean. The former has some structural similarity to, for example, annual-mean Sargasso Sea temperatures, but no credible claim for its relevance can be made in the absence of diabatic surface forcing.

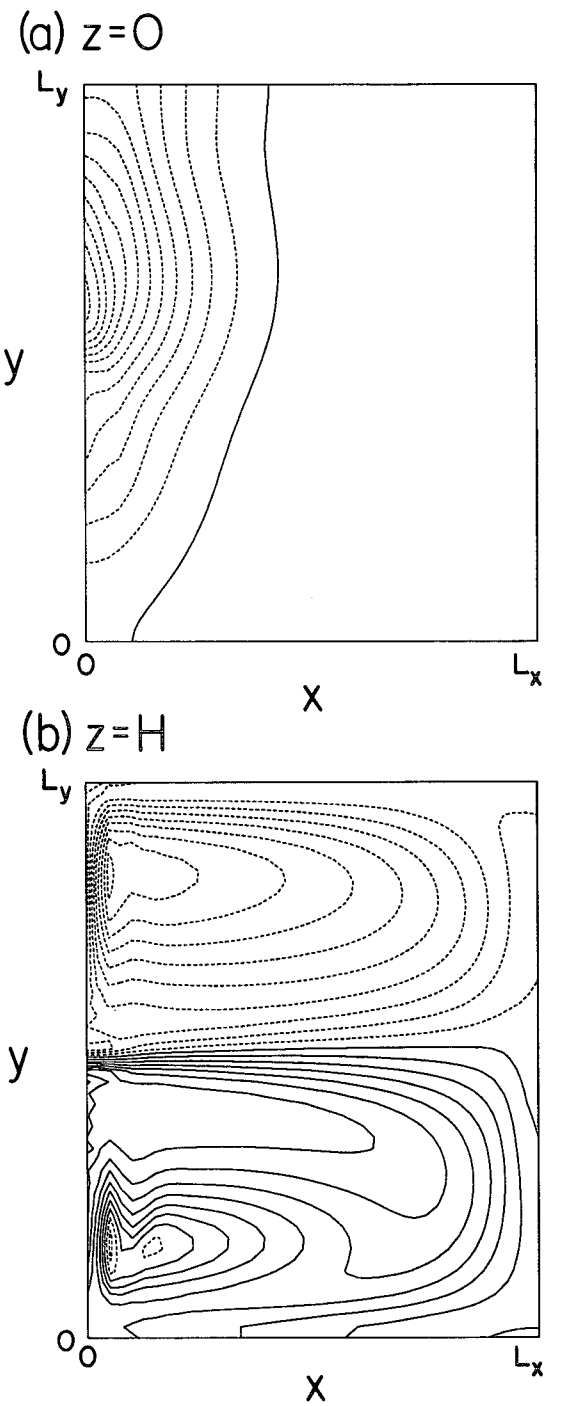

FIG. 8. Plot of $\theta(x, y)$ at $t = 200$ on the vertical boundaries, $z = 0$ and H, with contour intervals 1×10^{-4} and 0.05, respectively.

b. Solution sensitivities

Here we briefly report on the robustness of the preceding solution to various numerical and physical parameter variations and to the choice of dynamical model. The particular sensitivities associated with ν_v, nonlinearity, $S(z, 0)$, and $\kappa_i(x, y)$ are deferred to sections 4c–f.

The solution in section 4a is largely insensitive to variations in the numerical resolution in both space and time. The most substantial effect of finer spatial resolution is an intensification of the western boundary vertical-velocity extremum, as expected from its "delta-function" character (appendix A).

The solutions for the BE and LBE models are virtually indistinguishable for the present eddyless solutions, as might be expected from the smallness of their $R\zeta/f$ values (i.e., everywhere less than 0.05) that measure the divergent vorticity advection present in the BE. From this we infer that primitive equation solutions would also match the present ones nearly exactly, although we have not made the calculations to check this. For the simpler QG model, though, there are modest quantitative differences in almost all aspects of the solution. Compare, for example, the shallow and deep horizontal circulation patterns in Fig. 9 with their counterparts in Fig. 1. The qualitative differences in QG are an exact symmetry between the subtropical and subpolar gyres for the symmetric wind forcing (18)—the principal source of gyre asymmetry in LBE/BE is a more accurate treatment of the Coriolis force (see MNGH)—and the occurrence of isothermal top and bottom boundaries even with $\kappa_i \neq 0$, because of the absence of the second term in (11), which makes any $\kappa_h \neq 0$ irrelevant.

The stress/slip coefficient α in the viscous horizontal boundary condition (6d) and the horizontal viscosity ν_h influence the near-boundary flow profile as in the linear boundary-layer solution [e.g., (A6)], but they do not have a significant influence on the large-scale circulation. For these eddyless solutions with marginally inertial boundary currents, there is not the strong control of the separation dynamics seen in eddy-resolving solutions (Haidvogel et al. 1992). Similarly, an asymmetry in the strength of the wind between the two gyres simply affects each of the gyres internally, since there is not an inertial collision of the boundary currents at the line curl $\tau_s = 0$ as found in eddy-resolving solutions (MNGH). These insensitivities can be seen, therefore, as weaknesses of the parameterizations in the eddyless solutions.

Reductions in isopycnal diffusivity κ_i from its value in (20) lead to unstable, hence unsteady, solutions below a critical value of around 0.02 [i.e., 10^3 m^2 s^{-1} from (16)]. Increases in κ_i, on the other hand, lead to greater linearity of the solution, weaker energies and rates of working, larger boundary temperatures, and deeper penetration of the ψ and ξ circulations (e.g., Fig. 10), but with little change in the barotropic component. The value of κ_i also influences the western boundary-layer profile (appendix A). These tendencies, though, do not alter the qualitative character of the solutions.

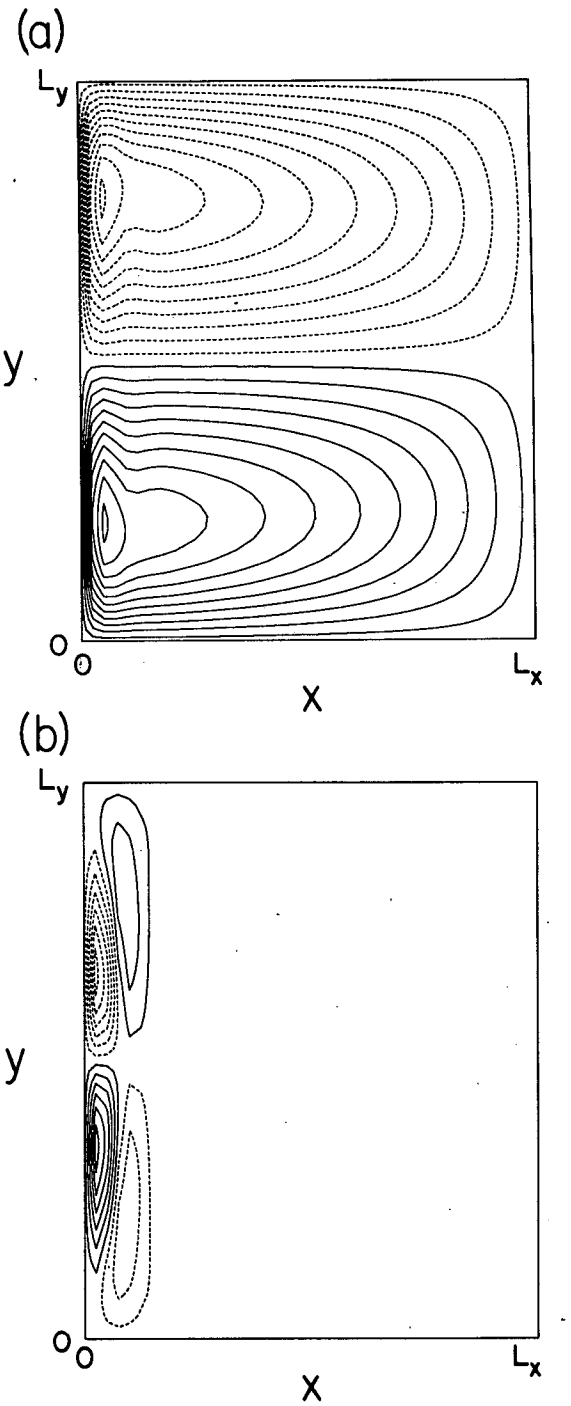

FIG. 9. Plot of $\psi(x, y, z_l)$, $l = 6$ and 1 for a QG solution at $t = 200$ analogous to the LBE solution in section 4a. The contour intervals are 0.1 and 0.005, respectively.

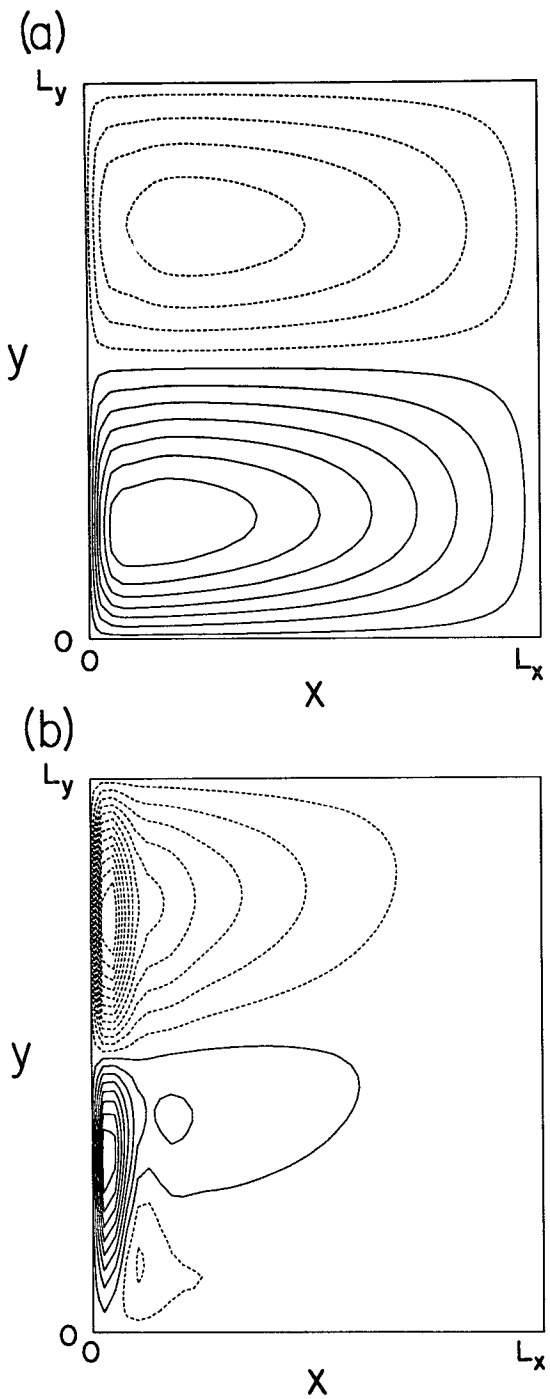

FIG. 10. Plot of $\psi(x, y, z_l)$, $l = 6$ and 1 for a LBE solution analogous to the one in section 4a, except for a larger $\kappa_i = 0.15$. The contour interval is the same as in Fig. 1 for $l = 6$, but it is twice as large, 0.01, for $l = 1$. The time is $t = 200$.

Finally, we can put the boundary buoyancy diffusivity κ_h to zero with virtually no change in the vertically interior circulation. This makes the solution adiabatic in an integral sense (i.e., quasi-adiabatic; see section 3) and, hence, exactly steady at late times: the small imbalance in P vanishes (cf. Fig. 6), but otherwise the energy budget is unchanged. However, the boundary temperature gradients forced by $\kappa_i \neq 0$ undergo the advective cascade to the smallest available horizontal scales without any limiting diffusion (section 3), and thus $\theta(H)$ has a larger extremum than in Fig. 8b by about a factor of 3 and is highly nonsmooth at late times. Together these properties clearly indicate the weakness of any influences of the boundary temperature on the interior circulation.

c. *Solutions with vertical viscosity*

As described in section 3, vertical viscosity can be expected to play a similar role to isopycnal diffusion. Here we consider solutions analogous to the one in section 4a, but with $\kappa_i = 0$ and $\nu_v \neq 0$. Again there is a critical value for steadyness at late times, somewhat above $\nu_v = 3$ [i.e., $\nu_{v*} \approx 0.4$ m^2 s^{-1} for a dimensionalization factor of $V_* h_*^2 / l_* = 0.13$ m^2 s^{-1} from (16)]. For ν_v values above critical, the solutions are indeed grossly similar to ones with $\kappa_i \neq 0$, but the correspondences are not quantitatively close. For example, for $\nu_v = 3.5$, the streamfunction field exhibits less gyre asymmetry and much weaker abyssal flow than in Fig. 1; larger ν_v would diminish vertical shear and thus exacerbate the former and ameliorate the latter.

The correspondences become stronger when the QG-equivalent form (12a) is used in LBE or BE solutions. Furthermore, with the PG-equivalent form (12b), the ψ field becomes very much like Fig. 1. Other solution properties differ, though. The energy balance (Fig. 11) is remarkably similar in all aspects except that kinetic energy dissipation by the vertical viscosity replaces

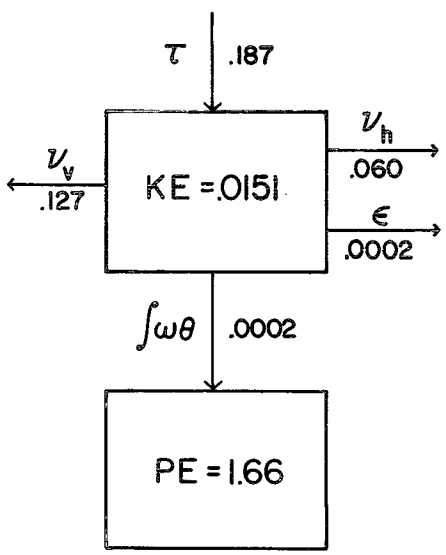

FIG. 11. Volume-integrated energetics at $t = 200$ for the solution in section 4c with a PG-equivalent vertical viscosity.

baroclinic conversion and potential energy dissipation by the isopycnal diffusivity. Note also that the imbalance in the potential energy budget [i.e., the temporal trend in PE associated with boundary diffusion of θ by κ_h in (15)] is an order of magnitude smaller than in Fig. 6. This is because the top-boundary θ field is much weaker here (Fig. 12) than in Fig. 8. Its source in (9) occurs only at O(R). When $Q_i = 0$ as here, the only source is the nonlinear divergent advection terms, since the O(1) rotational advection and diffusion terms cause only horizontal transport. Besides being weaker, the pattern in Fig. 12 differs from that in Fig. 8b by a positive extremum in the southwestern subpolar gyre; this greatly diminishes the strength of the gyre-boundary thermal front. We defer any assessment of which pattern is more correct, since as yet no boundary temperature fields from an eddy-resolving solution have been published. The overturning circulations for this solution with a PG-equivalent vertical viscosity (Fig. 13) are similar to those in Fig. 5, even though $\kappa_i = 0$ requires that they be due entirely to advective forcing here. The meridional circulation (Fig. 13a) lacks a central positive extremum in ξ^{yz}, but there is the same four-extremum pattern in the upper-ocean vertical velocity as in Fig. 5a; other differences here are less intense motions at the meridional boundaries and greater gyre asymmetry. The zonal circulations ξ^{xz} (Figs. 13b,c) are rather similar to those in Figs. 5b,c in the upper ocean, particularly away from the eastern boundary, but are much weaker in the deep ocean.

On the whole we find it remarkable that there is so much similarity in the ψ fields, given that the correspondence between spatially uniform isopycnal mixing and its "equivalent" vertical viscosity is formally only O(1) (section 3) and other O(R) effects that distinguish QG and LBE/BE solutions are clearly significant. The similarity is even more remarkable in both the ξ and boundary θ fields, where the isopycnal mixing terms make such a strong contribution when $\kappa_i \neq 0$. When $\kappa_i = 0$ and $\nu_v \neq 0$, nonlinear advection must provide the balances both to the rotational advection and horizontal diffusion of boundary temperature variations and to vertical velocity in the interior (hence ξ) in (9); thus, for more linear solutions as $\tau_0 \to 0$ (see section 4d), both $\theta(0, H)$ and ξ are O(τ_0^2), whereas ψ is O(τ_0). In contrast, for $\kappa_i \neq 0$, ξ is O(τ_0) because of the linear first term in (11), although $\theta(0, H)$ remains O(τ_0^2) since the nonlinear second term in (11) is the only contributor from Q_i on the vertical boundary, given (13).

d. A linear, quasigeostrophic analog

The parameters of the representative solution (section 4a) imply that the western-boundary currents are too strong for a linear solution to be accurate and the meridional extent of the basin is too large for a QG solution to be accurate (cf. Figs. 1 and 9). Nevertheless, even with both of these simplifications, many of the essential effects of κ_i are incorporated, and the solutions of the physically more accurate model differ more in degree than kind.

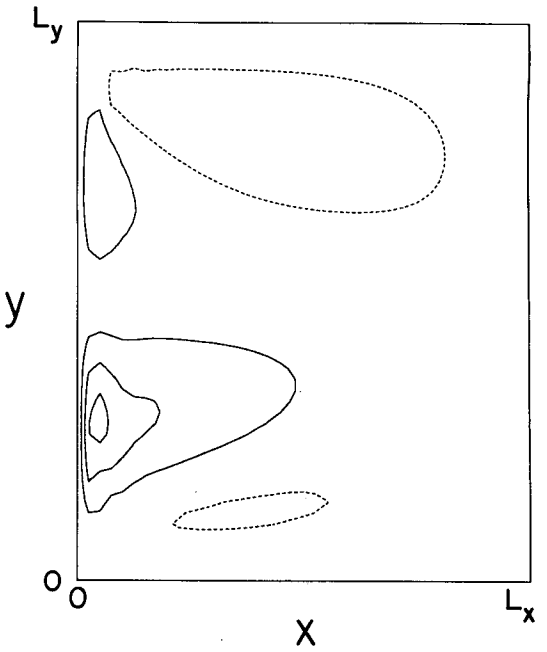

FIG. 12. Plot of $\theta(x, y)$ at $t = 200$ and $z = H$. For the solution in section 4c with a PG-equivalent vertical viscosity (12b), the contour interval is 0.05.

We can assure linear dynamics by making τ_0 sufficiently small, and $\tau_0 = 0.0625$ suffices. The resulting solutions for QG have the streamfunction patterns shown in Fig. 14. They are, of course, symmetric between the gyres (as in Fig. 9 also). Compared to both Figs. 1 and 9, in the linear solution there is a greater degree of surface intensification, an approximate separability of the functional dependences in x and y [as in the Sverdrup solution (21)], and no visible recirculation near the western boundary in the upper ocean but an enhanced recirculation in the deep ocean (relative to the weaker boundary current there). The circulations near the western boundary conform quite closely to the boundary-layer solutions of appendix A, given the $\Psi(y, z)$ that results from the interior dynamics of surface wind forcing and isopycnal mixing. Although there are quantitative differences with the nonlinear LBE and QG solutions of sections 4a,b, even beyond the rescaling in amplitude proportional to τ_0, the overturning circulations and energetics in the linear solution are qualitatively similar. Of course, the boundary θ fields are zero here (because $R = 0$), and the weakness of the circulation precludes the occurrence of any appreciable homogeneity in the large-scale potential vorticity (24).

e. Stratification and potential vorticity homogeneity

The tendency toward homogeneity in PV from (24) can be understood qualitatively from the gross structure

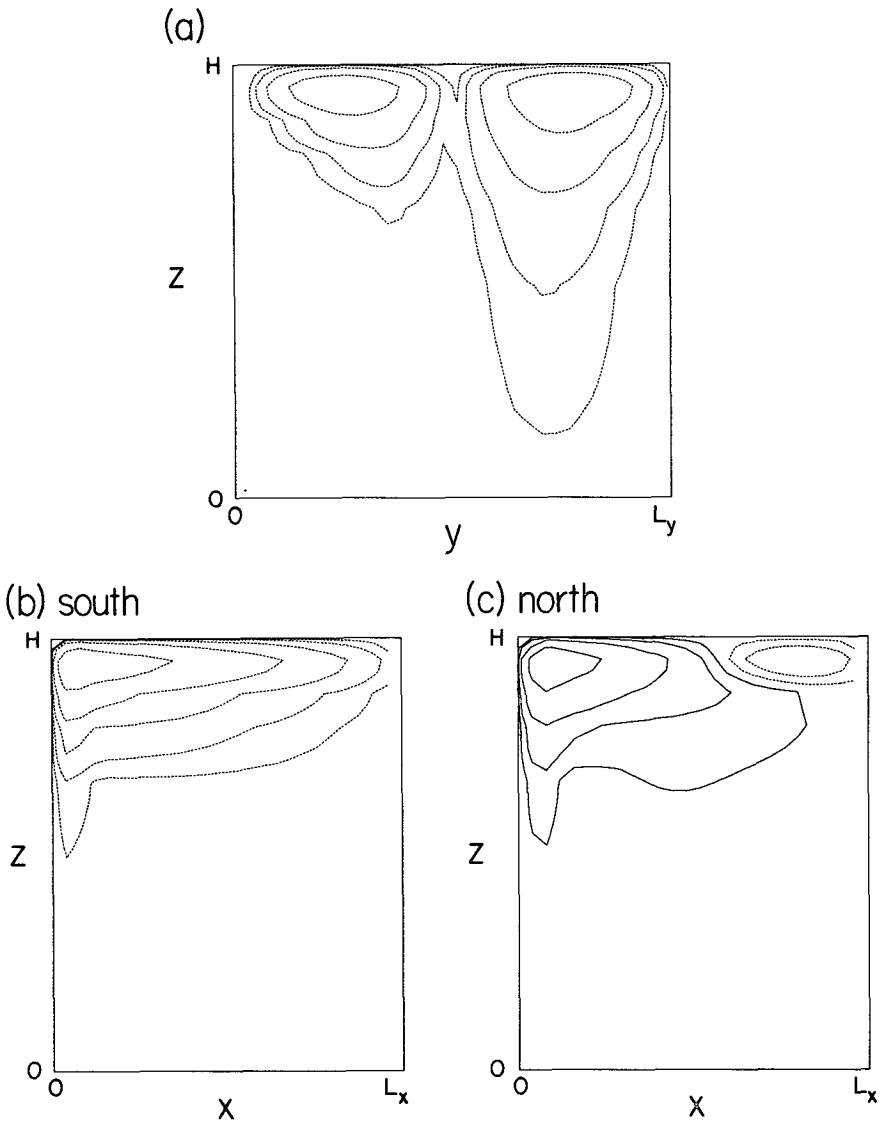

FIG. 13. The mean overturning circulations in the meridional and zonal planes for the solution in section 4c with a PG-equivalent vertical viscosity at $t = 200$: (a) $\xi^{(yz)}$, (b) and (c) $\xi^{(xz)}$ for the southern and northern halves of the domain. The contours begin at $\pm\sqrt{10} \times 10^{-2}$ and increase in magnitude geometrically by the factor $\sqrt{10}$.

of θ in the gyres: its magnitude is largest in the thermocline; in the subtropical gyre, θ is mostly positive, hence T_z is enhanced, hence the reduction in PV due to a smaller $f(y)$ in the south is opposed by a larger T_z; in the subpolar gyre, T_z is smaller but f is larger, so again their tendencies are opposing in Q. If one evaluates PV on an isopycnal surface, however, another effect comes into play: isopycnal surfaces are depressed in the subtropical gyre, and, if $S(z)$ is monotonically increasing with z, as in (19), then T_z will be correspondingly diminished there, thus countering the enhancement discussed above (and vice versa in the subpolar gyre). Thus, we interpret the considerable homogeneity of Q on level surfaces (Fig. 7a) as due to the first effect, and the lesser homogeneity on T surfaces (Fig. 7b) as a consequence of the second effect.

This suggests the hypothesis that $S(z)$ can influence strongly the homogenization of PV. (In our solutions, S is largely determined from its initial condition. Its fundamental origin is in the long-time diabatic dynamics neglected here.) To explore this hypothesis, we obtain a solution analogous to the one in section 4a but with an altered $\Theta(z, 0)$. The alteration is to create an isolated thermocline, such that its gradient S is enhanced below $z = z_* = 5.5$ and diminished above, with a shape such that the gravest baroclinic deformation

radius is unchanged from 45 km (see the inset panel in Fig. 15). This shape is qualitatively more realistic than the simple exponential form in (19); it also will reverse the second effect on PV due to variations in a T-surface depth discussed above. The resulting solution is qualitatively quite similar to the earlier one, except that the surface intensification of the circulation is diminished above the thermocline. Strikingly, though, PV is now much more homogeneous on an upper-thermocline T surface (Fig. 15b) than on a nearby z surface (Fig. 15a). Thus, the hypothesis of control of homogeneity by stratification is confirmed, and we have provided a cautionary illustration about inferring eddy mixing of potential vorticity from its approximate, large-scale homogeneity. [A quite different cautionary example is given in Williams (1991).]

f. Spatially variable diffusivities

Mesoscale eddy energy levels and diffusivities have substantial spatial variability in the ocean (e.g., McWilliams et al. 1983); therefore, an accurate parameterization should go beyond the uniform diffusivities we have considered thus far. Here we briefly examine two forms of nonuniform κ_i for their influence on one of the major deficiencies of the solution in section 4a, namely, the excessively broad meridional interval of separation for the upper-ocean western boundary currents (Fig. 1a).

A heuristically plausible form for κ_i is to be larger where the large-scale currents are stronger, presuming that the eddies that effect the mixing are stronger there because of enhanced instabilities. Thus, we consider

$$\kappa_i(x, y, z) = 0.01 + 0.1ke(x, y, z), \qquad (25)$$

where $ke = \frac{1}{2}(\nabla\psi)^2$. [Marshall (1984) made a similar proposal using independently diagnosed eddy potential enstrophy density instead of mean kinetic energy density.] The spatial maximum achieved by (25) is 0.42 in the narrow region of the upper, western-boundary current where the flow is strongest, and its minimum is close to 0.01 in the deep interior regions; thus, its values bracket the constant value in (20). In the dimensional form of (25), the coefficient of the last term is a time, $t = 0.1l_*/V_* \approx 6$ days. We do not know how to interpret this value beyond meeting the general requirement for some integral measure of κ_i to be large enough for the steady circulation to be stable. A comparison of solutions with (20) and (25) (i.e., Figs. 16a and 16b, respectively) shows that the separation structure is made worse, by being broader, with the ke-dependence in (25). The upper-ocean transport is also weaker with (25), which is consistent with the κ_i magnitude dependence in section 4b and Fig. 10.

In MNGH it was found that the baroclinic energy conversion from mean currents to eddies was generally positive in the interior and negative near the western boundary. Thus, an alternative plausible form for κ_i is to be diminished near the boundaries. (We avoid regions of $\kappa_i < 0$, for now at least, because of its possible ill-posedness in time integrations.) Another advantage of this form is that it smoothly approaches the hori-

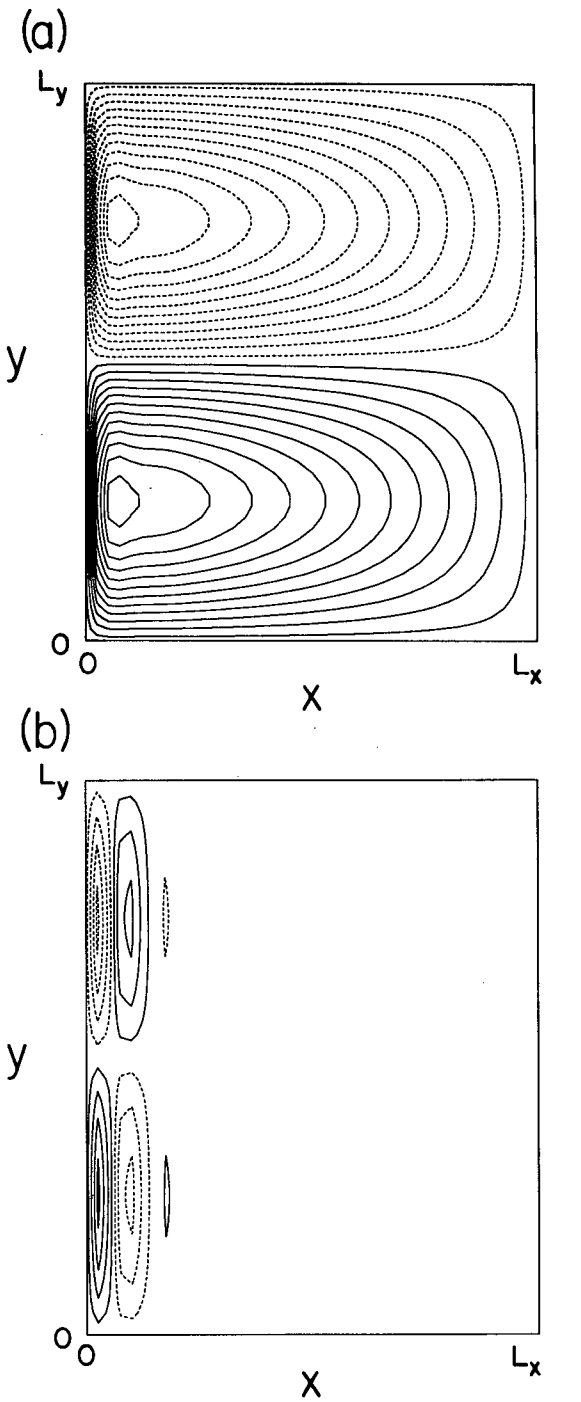

FIG. 14. Plot of $\psi(x, y, z_l)$, $l = 6$ and 1 for a QG solution analogous to the LBE solution in section 4a, except for a $\tau_0 = 0.0625$ smaller by a factor of 0.01. The contours are correspondingly reduced by a factor of 0.01 relative to those in Fig. 1.

zontal boundary condition in (13), in contrast to the abrupt approach for uniform diffusivity; this has the effect of broadening and weakening the vertical velocities in the boundary current (see appendix A). We achieve this form with taper functions near the horizontal boundaries:

$$\kappa_i(x, y) = 0.03W(x)W(L_x - x)W(y)W(L_y - y), \tag{26}$$

where the interior magnitude is as in (20) and the taper functions are defined by

$$W(s) = \tanh\left[\frac{s}{\Delta}\right] \tag{27}$$

with $\Delta = 0.6$ [i.e., 300 km from (16)]. The resulting solution (Fig. 16c) has a better (narrower) separation structure and larger upper-ocean transport [consistent with smaller overall κ_i in (27)].

We can also examine the combination of these influences with the following diffusivity form:

$$\kappa_i(x, y, z) = [0.01 + 3.0ke(x, y, z)]\tilde{W}(x) \times W(L_x - x)W(y)W(L_y - y), \tag{28}$$

where there is an even more severe taper function near the western boundary; namely,

$$\tilde{W}(s) = 0, \; s \leq \Delta$$
$$= \tanh\left(\frac{s - \Delta}{\Delta}\right), \; s > \Delta, \tag{29}$$

with the same $\Delta = 0.6$. The spatial maximum value for (28) is 0.17 and it occurs in a broad offshore region (centered at $x \approx 3\Delta$, $y \approx L_y/2$); the spatial minimum value, of course, is zero near the western boundary. The larger coefficient for *ke* in (28), compared to (25), arises because the region in which κ_i is most important is now offshore where *ke* is much smaller; again, the primary consideration appears to be having big enough κ_i in some integral sense. The separation structure of the solution (Fig. 16d) is now even better (narrower and stronger) than with a taper alone (Fig. 16c), and the *ke* dependence aids in this rather than opposes it as when it acts alone [as in (25) and Fig. 16b].

Thus, there is an appreciable sensitivity to spatial variations in diffusivity, and there is good reason to explore this behavior further.

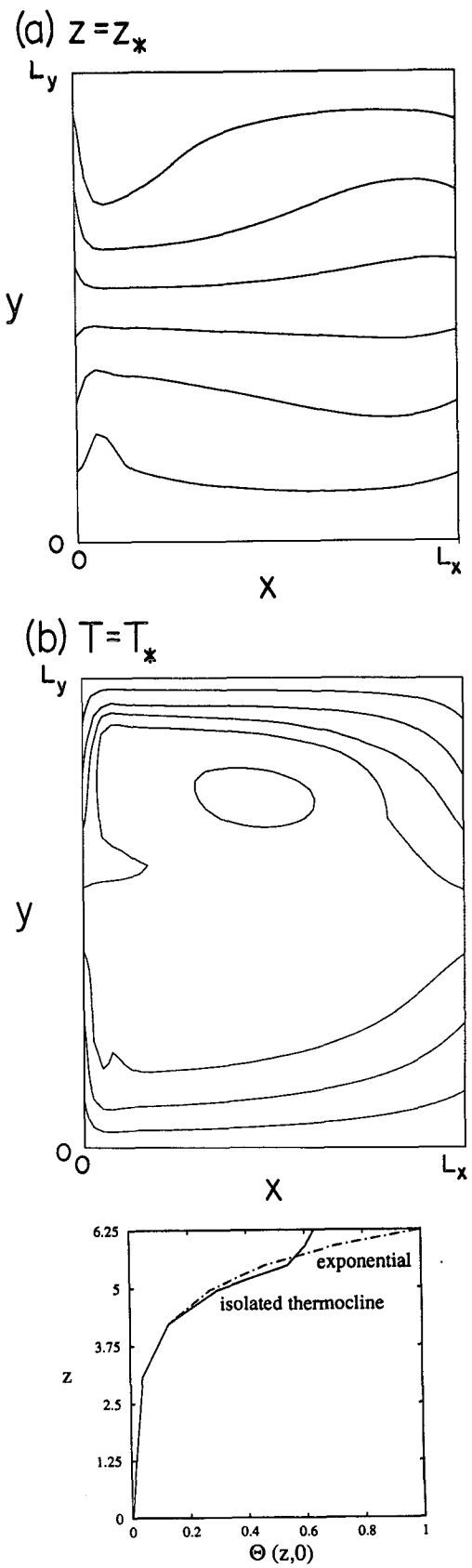

FIG. 15. Large-scale potential vorticity (24) at $t = 200$ for the solution with an isolated thermocline in $\Theta(z, 0)$ [see inset, which also includes (19)]: (a) PV(x, y, z_*) for $z_* = 5.48$; (b) PV(x, y, T_*) for $T_* = 4.2$ (the horizontal average height of this T_* surface is 5.44). The contours have an interval of 150 and straddle the average value.

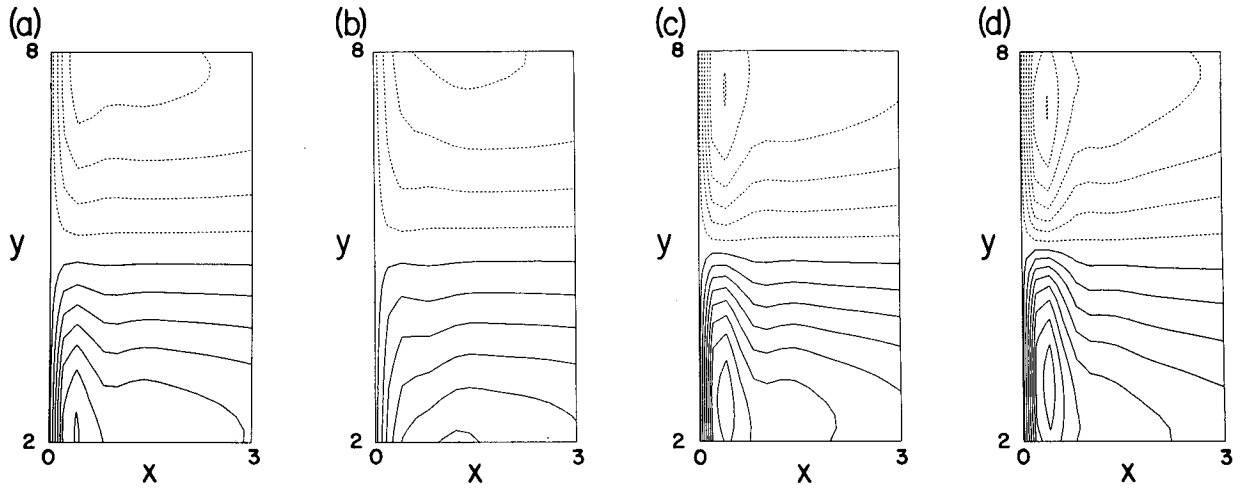

FIG. 16. Near-surface circulation, $\psi(x, y, z_6)$, in a region near the central western boundary ($0 < x < 3$, $2 < y < 8$) for solutions with different $\kappa_i(x, y)$: (a) constant [as in section 4a; see (20)]; (b) dependent upon kinetic energy density [see (25)]; (c) tapered near the boundary [see (26)-(27)]; and (d) with both effects as in (28)-(29). The contours have an interval of 0.2 and straddle zero.

5. Discussion

The solutions presented in section 4 show that the isopycnal-thickness mixing parameterization of GM90 with a realistic diffusivity magnitude can quasi-adiabatically balance the surface wind driving with a large-scale circulation pattern of approximately the right magnitude and horizontal and vertical scales. Furthermore, the suite of solutions examined shows that this behavior is robust with respect to model and parameter variations. Also, as in MNGH, it is found that the greater dynamical fidelity of balanced dynamics, compared to the simpler quasigeostrophic dynamics, provides a significant improvement in accuracy for the oceanic general circulation. Additional, specific findings are the following: our isopycnal parameterization and an unphysically large vertical viscosity with the particular functional dependence in (12a) can yield broadly similar circulation patterns, and the mean static-stability profile significantly influences the degree of homogeneity of large-scale potential vorticity on level and isopycnal surfaces.

Our broad goals in this context are to develop mesoscale eddy parameterizations suitable for use in realistically configured, eddyless, oceanic general circulation models and to develop balanced models both as a conceptual framework and as a possible computational basis for these dynamics. The present results contribute to both goals. There remains, however, an important missing element even in the idealized problems solved here. A parameterization is accurate only if its eddyless solutions correspond closely to the spatially and temporally filtered component of eddy-resolving solutions. We make no such claim for the present eddyless solutions and have avoided making any detailed comparisons here. It is clear that in certain gross features, such as the separation dynamics of the western boundary current and the eddy-driven recirculation zone, there are substantial discrepancies between eddyless and eddy-resolving solutions. The missing element in the present parameterizations is spatial and/or flow-configuration dependence of the diffusivities. No doubt this property is as necessary for ν_h as for κ_i since the horizontal Reynolds stresses by mesoscale eddies are also quite inhomogeneous in their effects (e.g., see MNGH). We have shown some aspects of solution sensitivity to nonuniform diffusivities (section 4f) but, as yet, do not have a serious proposal for what form this dependence ought to take. We hope to address this issue in the future, along with the many other extensions required to move from highly idealized problems to more realistic ones for oceanic general circulation models.

Acknowledgments. Programming, computations, and preparation of appendix B were accomplished with the able assistance of Nancy Norton. This research was sponsored by the National Science Foundation through Contract OCE-9012754 and its contract with the National Center for Atmospheric Research.

APPENDIX A

Linear Western Boundary Layers

Here we present solutions with the approximations of time-independence and linearity and with a boundary-layer structure near the western boundary. Such solutions are extensions of the classical, barotropic solutions of Stommel (1948) and Munk (1950) to our baroclinic situation with nonzero ϵ, ν_h, α, κ_i, and/or ν_v, and we will show that they contain several features also found in the 3D nonlinear solutions of section 4.

We define a boundary-layer coordinate, $\eta \equiv x/\mu$ with $\mu \ll 1$ and assume that the solution in the vicinity of

$x = 0$ is a multiscale function of (x, η, y, z), such that all (x, y) derivatives are negligible compared to η derivatives. Thus, we can write the local streamfunction as

$$\psi(x, \eta, y, z) = \Psi(z) + \tilde{\psi}(\eta, z), \qquad \text{(A1)}$$

where Ψ is the streamfunction profile just outside the boundary layer as established at this particular y by the interior dynamics related to the wind driving; thus, any mutual dependencies between the boundary layer and interior are neglected in this analysis. Since ν_h is relatively large among the various diffusivities, we use it to define the boundary-layer scale $\mu = (\nu_h/\beta)^{1/3}$ [$= 0.153$ for the parameters in (17)], as in the Munk solution. The resulting boundary value problem for $\tilde{\psi}$ is the following:

$$\frac{\partial^4\tilde{\psi}}{\partial\eta^4} - \frac{\partial\tilde{\psi}}{\partial\eta} = -\frac{\partial}{\partial z}\left(\frac{1}{S(z)}\frac{\partial}{\partial\eta}K(\eta, z) + V(\eta, z)\frac{\partial}{\partial\eta}\right)\frac{\partial^2\tilde{\psi}}{\partial z\partial\eta}, \qquad \text{(A2)}$$

with boundary conditions

$$\tilde{\psi} = -\Psi, \quad \frac{\partial^2\tilde{\psi}}{\partial\eta^2} = A\frac{\partial\tilde{\psi}}{\partial\eta}, \quad K\frac{\partial^2\tilde{\psi}}{\partial z\partial\eta} = 0 \quad \text{at} \quad \eta = 0$$

$$\tilde{\psi} \to 0 \quad \text{as} \quad \eta \to \infty$$

$$V\frac{\partial^3\tilde{\psi}}{\partial z\partial\eta^2} = E\frac{\partial^2\tilde{\psi}}{\partial\eta^2}, \quad K = 0 \quad \text{at} \quad z = 0$$

$$V\frac{\partial^3\tilde{\psi}}{\partial z\partial\eta^2} = 0, \quad K = 0 \quad \text{at} \quad z = H, \qquad \text{(A3)}$$

where

$$V \equiv \nu_v\mu^2/\nu_h, \quad A \equiv \alpha\mu,$$

$$K \equiv \kappa_i\mu^2/\nu_h, \quad E \equiv \epsilon\mu^2/\nu_h. \qquad \text{(A4)}$$

Associated with $\tilde{\psi}$ are the meridional and vertical velocities,

$$v = \mu^{-1}\frac{\partial\tilde{\psi}}{\partial\eta}, \quad w = \frac{\beta}{\mu}\frac{1}{S(z)}\frac{\partial}{\partial\eta}\left(K(\eta, z)\frac{\partial^2\tilde{\psi}}{\partial z\partial\eta}\right). \qquad \text{(A5)}$$

Note that w, hence $\xi^{(xz)}$ in (23), can be nonzero in this dynamics only if $\kappa_i \neq 0$.

For the special case of $V = K = E = 0$, the solution of (A2)–(A4) has an η dependence as in the Munk solution with only a parametric dependence on z:

$$\tilde{\psi} = -\Psi(z)e^{-\eta/2}\left(\cos\frac{\sqrt{3}\eta}{2} + \frac{1}{\sqrt{3}}\frac{A-1}{A+1}\sin\frac{\sqrt{3}\eta}{2}\right). \qquad \text{(A6)}$$

For any of V, K, or E nonzero, the boundary-value problem is fully two-dimensional, hence analytically difficult, and we obtain numerical solutions based upon the same spatial-discretization formulas used for the general model.

For $E \neq 0$ but $V = K = 0$, then only at the lowest level is $\tilde{\psi}$ changed from (A6), and the primary effect is to expand the boundary-layer width. However, for the parameter values in (17), $E = 0.26$, and the departures from (A6) are quite modest.

For $\tilde{\psi}^z$, all effects from K and V disappear; thus, the boundary-layer prediction for the barotropic streamfunction only differs from (A6) [with $\Psi = \psi_{sv}(0, y)$] by a negligible correction proportional to E.

The κ_i value of (20) implies $K = 0.00466$. A boundary-layer solution with these K and E values is shown

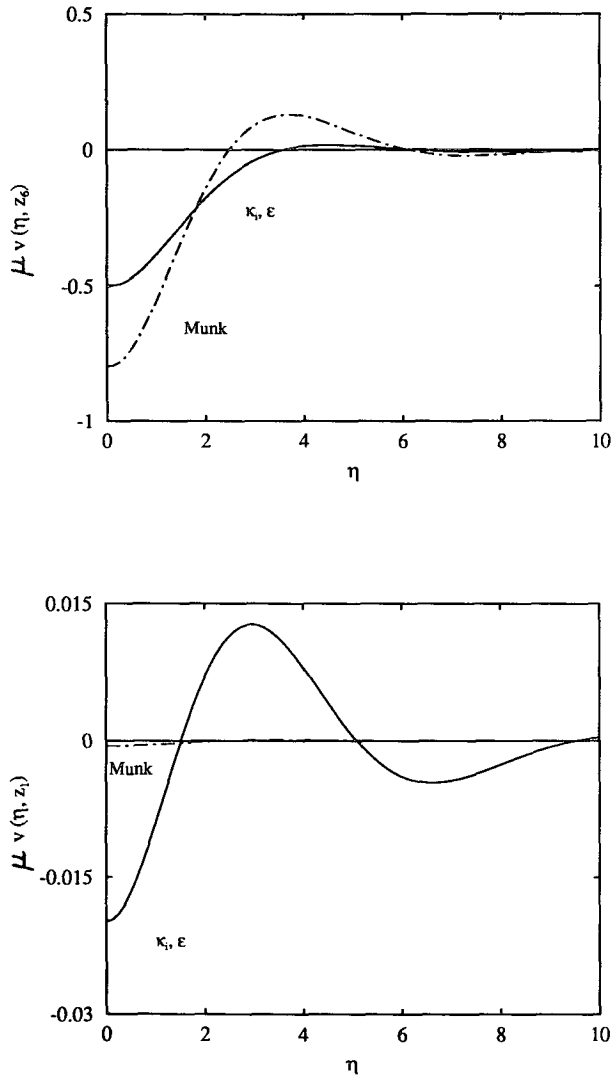

FIG. A1. Boundary-layer velocity profiles $v(\eta, z_l)$, $l = 6$ and 1 for both a Munk-like solution (A6) and one with ϵ and $\kappa_i \neq 0$ (i.e., $E = 0.26$ and $K = 0.00466$). The interior profile $\Psi(z)$ is taken from the middle latitude of the subpolar gyre in the solution of section 4a.

in Fig. A1. Relative to (A6), the upper-ocean velocity profile is weaker and broader in distance to the first stagnation line and is weaker in its secondary extrema. In the deep ocean, in contrast, the velocities are strengthened relative to (A6)—greatly, in this instance, because $\Psi(z)$ decays so strongly with depth, by $\sim 10^{-3}$ between top and bottom—narrower between stagnation lines, and relatively much stronger in the secondary extrema. The associated vertical velocity (A5) has $\int d\eta w = 0$ from the boundary conditions in (A3). The $\eta = 0$ boundary condition also implies a strong forcing for w at the boundary, since neither K nor $\partial\tilde{\psi}/\partial\eta$ smoothly approaches zero as $\eta \to 0$; at all interior grid points, however, $K(\partial\tilde{\psi}/\partial\eta)$ is smoothly varying, and therefore w is much smaller. Thus, there is a "delta-function" character to $w(\eta)$, with strong motion of one sign at the boundary and a broad interval of weaker motion of the opposite sign in the interior (as in Figs. 5b,c); as the grid interval is reduced, the magnitude of the wall extremum increases but its contribution to the vertical transport does not. [Note that this delta-function forcing does not appear in the potential vorticity equation (A2) for $\tilde{\psi}$, which is only evaluated at interior grid points since the boundary value problem is of Dirichlet type in η.] The vertical structure of w is controlled by that of Ψ through $\tilde{\psi}$. Because of the S^{-1} factor in (A5), an exponential profile for Ψ with decay scale $\Delta z \sim 1$ implies a w with only weak depth dependence; thus, the surface intensification of w (Figs. 5b,c) is a consequence of Ψ being more surface intensified than e^{z-H}.

These effects are typical, varying only in degree with K and Ψ. In particular, the relatively stronger deep horizontal circulation in the subpolar gyre (Fig. 1b), as well as the relatively deeper zonal overturning circulation there (Figs. 5b,c), are qualitatively captured in our boundary-layer solutions as a consequence of the lesser degree of surface intensification of the subpolar gyre.

For $K = K(\eta)$ increasing smoothly from zero at the boundary to a uniform interior value, the w profile loses its delta-function character and becomes independent of grid resolution for fine grids. However, the signs of the near-boundary and interior w are the same as for uniform K.

Finally, solutions with $K = 0$ and V from (12a) are quite similar in both $\tilde{\psi}$ and v to the profiles in Fig. A1 (as in section 4c), but they differ grossly in w, which is zero with $K = 0$ by (A5).

APPENDIX B

Discretization Formulas for Q_i and Q_h

In this section the discrete forms of the BE diabatic terms in (8)–(9) are presented using the operator notation presented in MNGH appendix A. We review only those operators from MNGH that are used in our definitions of the discrete forms of (11) and (14). The first is the vertical difference operator

$$\mathcal{V}_k^{(2)}[C] = \frac{s'_{2k}}{2ds}(C_{k+1} - C_{k-1}), \quad k = 1, 2, \cdots, N_z - 1$$

$$\mathcal{V}_k^{(2)}[C] = \begin{cases} \dfrac{-s'_{2k}}{ds} C_{k-1}, & k = N_z \\ \dfrac{s'_{2k}}{ds} C_{k+1}, & k = 0, \end{cases} \tag{B1}$$

where C is any dependent variable, s is the vertical stretching function in MNGH (23), and k is the discrete vertical k grid defined in the text that follows MNGH (23).

We use two horizontal operators to describe (11) and (14):

$$\begin{aligned}
\nabla\cdot C\nabla D|_{(i,j)\in\{I\}} &= \frac{1}{(da)^2}[(C_{i+1,j} + C_{i,j})(D_{i+1,j} - D_{i,j}) + (C_{i-1,j} + C_{i,j})(D_{i-1,j} - D_{i,j}) \\
&\quad + (C_{i,j+1} + C_{i,j})(D_{i,j+1} - D_{i,j}) + (C_{i,j-1} + C_{i,j})(D_{i,j-1} - D_{i,j})] \equiv \mathcal{D}[C, D], \\
\nabla\cdot C\nabla D|_{(i,j)\in\{b\}} &= \frac{1}{2(da)^2}[2(C_{n,s} + C_{n-1,s})(D_{n-1,s} - D_{n,s}) + (C_{n,s+1} + C_{n,s})(D_{n,s+1} - D_{n,s}) \\
&\quad + (C_{n,s-1} + C_{n,s})(D_{n,s-1} - D_{n,s})] \\
\nabla\cdot C\nabla D|_{(i,j)\in\{c\}} &= \frac{1}{(da)^2}[(C_{n,s+1} + C_{n,s})(D_{n,s+1} - D_{n,s}) + (C_{n,s-1} + C_{n,s})(D_{n,s-1} - D_{n,s})],
\end{aligned} \tag{B2}$$

and

$$\begin{aligned}
\nabla C\cdot\nabla D|_{(i,j)\in\{I\}} &= \frac{1}{2(da)^2}\{(C_{i+1,j} - C_{i,j})(D_{i+1,j} - D_{i,j}) + (C_{i-1,j} - C_{i,j})(D_{i-1,j} - D_{i,j}) \\
&\quad + (C_{i,j+1} - C_{i,j})(D_{i,j+1} - D_{i,j}) + (C_{i,j-1} - C_{i,j})(D_{i,j-1} - D_{i,j})\} \equiv \mathcal{H}[C, D] \\
\nabla C\cdot\nabla D|_{(i,j)\in\{b\}} &= \frac{1}{(da)^2} C_{n-1,s} D_{n-1,s} \\
\nabla C\cdot\nabla D|_{(i,j)\in\{c\}} &\equiv 0,
\end{aligned} \tag{B3}$$

where $\{I\}$ is the set of all horizontal interior points; $\{b\}$ is the set of all horizontal boundary points, excluding corner points; $\{c\}$ is the set of all corner points; n is the outward normal index; and s is the counterclockwise tangential index.

Discrete forms of (11) and (14) are thus represented on the k grid as follows:

$$Q_i = \mathcal{D}[\kappa_i, T] + \mathcal{V}^{(2)}\left[\frac{\kappa_i \mathscr{H}[T, T]}{\mathcal{V}^{(2)}[T]}\right], \quad \text{(B4)}$$

$$Q_h = \mathcal{D}[\kappa_h, T]\{\delta_{0,k} + \delta_{N_z,k}\}. \quad \text{(B5)}$$

REFERENCES

Gent, P. R., and J. C. McWilliams, 1983a: Regimes of validity for balanced models. *Dyn. Atmos. Oceans,* **7,** 167–183.

——, and ——, 1983b: Consistent balanced models in bounded and periodic domains. *Dyn. Atmos. Oceans,* **7,** 67–93.

——, and ——, 1990: Isopycnal mixing in ocean circulation models. *J. Phys. Oceanogr.,* **20,** 150–155.

Greatbatch, R. J., and K. G. Lamb, 1990: On parameterizing vertical mixing of momentum in non-eddy-resolving ocean models. *J. Phys. Oceanogr.,* **20,** 1634–1637.

Gregg, M. C., 1987: Diapycnal mixing in the thermocline: A review. *J. Geophys. Res.,* **92,** 5249–5286.

Haidvogel, D. B., J. C. McWilliams, and P. R. Gent, 1992: Boundary current separation in a quasigeostrophic, eddy-resolving ocean circulation model. *J. Phys. Oceanogr.,* **22,** 882–902.

Holland, W. R., 1986: Quasigeostrophic modeling of eddy-resolved ocean circulation. *Advanced Physical Oceanographic Numerical Modeling,* J. J. O'Brien, Ed., Reidel, 203–231.

——, T. Keffer, and P. B. Rhines, 1984: Dynamics of the oceanic general circulation: The potential vorticity field. *Nature,* **308,** 698–705.

Ierley, G. R., and W. R. Young, 1983: Can the western boundary layer affect the potential vorticity distribution in the Sverdrup interior of a wind gyre? *J. Phys. Oceanogr.,* **13,** 1753–1763.

Lorenz, E. N., 1967: *The Nature and Theory of the General Circulation of the Atmosphere.* World Meteorological Organization, 161 pp.

McDowell, S., P. B. Rhines, and T. Keffer, 1982: Maps of North Atlantic potential vorticity, and its relation to the general circulation. *J. Phys. Oceanogr.,* **12,** 1417–1436.

McWilliams, J. C., and J. H. S. Chow, 1981: Equilibrium geostrophic turbulence. I: A reference solution in a β-plane channel. *J. Phys. Oceanogr.,* **11,** 921–949.

——, and others, 1983: The local dynamics of eddies in the western North Atlantic. *Eddies in Marine Science,* A. R. Robinson, Ed., Springer-Verlag, 92–113.

——, N. J. Norton, P. R. Gent, and D. B. Haidvogel, 1990: A linear balance model of wind-driven, midlatitude ocean circulation. *J. Phys. Oceanogr.,* **20,** 1349–1378.

Marshall, J. C., 1981: On the parameterization of geostrophic eddies in the ocean. *J. Phys. Oceanogr.,* **11,** 257–271.

——, 1984: Eddy-mean-flow interaction in a barotropic ocean model. *Quart. J. Roy. Meteor. Soc.,* **110,** 573–590.

Munk, W. H., 1950: On the wind-driven ocean circulation. *J. Meteor.,* **7,** 79–93.

Norton, N. J., J. C. McWilliams, and P. R. Gent, 1986: A numerical model of the balance equations in a periodic domain and an example of balanced turbulence. *J. Comput. Phys.,* **67,** 439–471.

Redi, M. H., 1982: Oceanic isopycnal mixing by coordinate rotation. *J. Phys. Oceanogr.,* **12,** 87–94.

Rhines, P. B., 1977: The dynamics of unsteady currents. *The Sea, Vol. 6, Marine Modeling,* E. D. Goldberg, I. N. McCave, J. J. O'Brien, and J. H. Steele, Eds., Wiley, 189–318.

——, and W. R. Young, 1982a: Homogenization of potential vorticity in planetary gyres. *J. Fluid Mech.,* **122,** 347–367.

——, and W. R. Young, 1982b: A theory of the wind-driven circulation. I. Mid-ocean gyres. *J. Mar. Res.,* **40**(Suppl.), 559–596.

Stommel, H., 1948: The westward intensification of wind-driven ocean currents. *Trans. Amer. Geophys. Union,* **29,** 202–206.

Sverdrup, H. U., 1947: Wind-driven currents in a baroclinic ocean; with application to the equatorial currents of the eastern Pacific. *Proc. Natl. Acad. Sci.,* **33,** 318–326.

Welander, P., 1966: A two-layer frictional model of wind-driven motion in a rectangular ocean basin. *Tellus,* **18,** 54–62.

Williams, R. G., 1991: The role of the mixed layer in setting the potential vorticity of the main thermocline. *J. Phys. Oceanogr.,* **21,** 1803–1814.

Young, W. R., and P. B. Rhines, 1982: A theory of the wind-driven circulation. II. Gyres with western boundary layers. *J. Mar. Res.,* **40,** 849–872.